# Generation and Characterization of a Cell Type-Specific, Inducible Cre-Driver Line to Study Olfactory Processing

JNeurosci
THE JOURNAL OF NEUROSCIENCE

*Research Articles: Systems/Circuits*

# Generation and characterisation of a cell-type specific, inducible Cre-driver line to study olfactory processing

https://doi.org/10.1523/JNEUROSCI.3076-20.2021

**Cite as:** J. Neurosci 2021; 10.1523/JNEUROSCI.3076-20.2021

Received: 7 December 2020
Revised: 28 May 2021
Accepted: 1 June 2021

# Generation and characterisation of a cell-type specific, inducible Cre-driver line to study olfactory processing

Abbreviated title: Mitral cell-specific inducible Cre-driver line

Anzhelika Koldaeva[1†], Cary Zhang[1†], Yu-Pei Huang[1†], Janine K Reinert[1], Seiya Mizuno[2], Fumihiro Sugiyama[2], Satoru Takahashi[2], Taha Soliman[1], Hiroaki Matsunami[3], Izumi Fukunaga[1*]

[1]Sensory and Behavioural Neuroscience Unit, Okinawa Institute of Science and Technology Graduate University
[2]Laboratory Animal Resource Center, Tsukuba University
[3]Department of Molecular Genetics and Microbiology and Department of Neurobiology, Duke University

[†]These authors contributed equally.
* To whom correspondence should be addressed (Izumi.fukunaga@oist.jp).

**Abstract**

In sensory systems of the brain, mechanisms exist to extract distinct features from stimuli to generate a variety of behavioural repertoires. These often correspond to different cell types at various stages in sensory processing. In the mammalian olfactory system, complex information processing starts in the olfactory bulb, whose output is conveyed by mitral and tufted cells (MCs and TCs). Despite many differences between them, and despite the crucial position they occupy in the information hierarchy, Cre-driver lines that distinguish them do not yet exist. Here, we sought to identify genes that are differentially expressed between MCs and TCs of the mouse, with an ultimate goal to generate a cell-type specific Cre-driver line, starting from a transcriptome analysis using a large and publicly available single-cell RNA-seq dataset (Zeisel et al., 2018). Many genes were differentially expressed, but only a few showed consistent expressions in MCs and at the specificity required. After further validating these putative markers using *in-situ* hybridization, two genes, namely *Pkib* and *Lbdh2*, remained as promising candidates. Using CRISPR/Cas9-mediated gene editing, we generated Cre-driver lines and analysed the resulting recombination patterns. This indicated that our new inducible Cre-driver line, *Lbhd2-CreERT2*, can be used to genetically label MCs in a tamoxifen dose-dependent manner, both in male and female mice, as assessed by soma locations, projection patterns and sensory-evoked responses *in vivo*. Hence this is a promising tool for investigating cell-type specific contributions to olfactory processing and demonstrates the power of publicly accessible data in accelerating science.

**Significance statement**

In the brain, distinct cell types play unique roles. It is therefore important to have tools for studying unique cell types specifically. For the sense of smell in mammals, information is processed first by circuits of the olfactory bulb, where two types of cells, mitral cells and tufted cells, output different information. We generated a transgenic mouse line that enables mitral cells to be specifically labelled or manipulated. This was achieved by looking for genes that are specific to mitral cells using a large and public gene expression dataset,

and creating a transgenic mouse using the gene editing technique, CRISPR/Cas9. This will allow scientists to better investigate parallel information processing underlying the sense of smell.

## Introduction

The complexity of the brain, in part, originates from the diversity of its components, the rich variety of cells. This diversity is evident in morphology, connectivity, molecular expression profiles, and biophysical properties (Sanes and Masland, 2015; Zeng and Sanes, 2017; Luo et al., 2018), which together give rise to what we refer to as cell types. Because the differences are thought to reflect distinct computational tasks or functions (Masland, 2004; Luo et al., 2018), the ability to selectively identify, and to manipulate, each cell type experimentally is key to understanding how the brain works.

In rodents, complex, synaptic processing of olfactory information in the brain first occurs in the olfactory bulb. The principal cells of the olfactory bulb, the MCs and TCs, convey the output of this region and are thought to form parallel information streams. They differ in a variety of anatomical and physiological properties (Fukunaga et al., 2012; Igarashi et al., 2012; Phillips et al., 2012; Otazu et al., 2015; Economo et al., 2016; Kapoor et al., 2016; Jordan et al., 2018). MCs, which are the larger of the two, are thought to form distinct circuits with local neurons from those formed by TCs (Mori et al., 1983; Fukunaga et al., 2012; Phillips et al., 2012; Geramita et al., 2016), some of which may explain the differences in how they encode odors. For example, in TCs, the timing of responses adheres strictly to a specific phase of the sniff cycle, while MCs modulate the timing widely over the entire sniff cycle (Fukunaga et al., 2012; Igarashi et al., 2012; Ackels et al., 2020). Signal integration over this long temporal window is thought to allow MCs to represent more complex information (Fukunaga et al., 2012). Further, in contrast to TCs whose axons project to a more limited portion of the olfactory cortex, the target areas of MCs range widely, extending as far as the posterior piriform cortex, the cortical amygdala, and the lateral entorhinal cortex (Haberly and Price, 1977; Igarashi et al., 2012), indicative of a variety of behavioural contexts in which MCs are likely to be important.

Despite the fundamental roles these two cell types play in olfaction, suitable molecular markers and genetic tools are lacking. Molecules commonly used to label the output neurons of the olfactory bulb include protocadherin-21 (Nagai et al., 2005), T-box transcription factor 21 (*Tbx21*, also known as *Tbet*; (Papaioannou and Silver, 1998; Faedo et al., 2002)), as well as cholecystokinin (*Cck*) (Seroogy et al., 1985). In the brain, Tbx21 is expressed from embryonic day 14 (Faedo et al., 2002) and is exclusive to the principal neurons of the olfactory bulb, labeling both MCs and TCs (Faedo et al., 2002; Mitsui et al., 2011; Haddad et al., 2013). In contrast, *Cck* is expressed widely in the brain (Larsson and Rehfeld, 1979; Taniguchi et al., 2011). In the olfactory bulb, expression occurs preferentially in TCs over MCs (Seroogy et al., 1985), which has been utilized for analysing the unique physiology of TCs (Economo et al., 2016; Short and Wachowiak, 2019). These overlapping but differential expression patterns between *Cck* and *Tbx21* may be useful in discovering more selective markers to distinguish the two types of principal neurons.

A variety of methods now exist to analyse gene expression patterns in relation to cell types, including *in-situ* hybridization (Lein et al., 2006), as well as transcriptomic approaches that retain spatial information, with increasing resolution (Ståhl et al., 2016). More recently, single-cell RNA sequencing (scRNA-seq) (Sugino et al.,

2006; Tang et al., 2009; Pfeffer et al., 2013; Zeisel et al., 2015; Shekhar et al., 2016; Tasic et al., 2016) has seen rapid developments, which have enabled the investigation of cell-type specific gene expression patterns with unprecedented levels of detail and scale (Lein et al., 2017; Zeng and Sanes, 2017). A useful application of this information in turn may be to generate transgenic driver lines, that allow a particular cell type to be extensively studied. The availability of Cre-driver lines has been instrumental in revealing unique functions of distinct cell types, across multiple levels of analyses (Gong et al., 2003; Taniguchi et al., 2011; Madisen et al., 2012; Dhande et al., 2013; Cruz-Martín et al., 2014; Wolff et al., 2014; Madisen et al., 2015; Sanes and Masland, 2015; Daigle et al., 2018).

Here, we take advantage of a large dataset that has become publicly available (Zeisel et al., 2018), to discover markers that distinguish between MCs from TCs. The results of the analyses allowed us to generate, and characterize, new Cre-driver lines. Such molecular tools will be key to understanding the mechanisms of olfactory perception and behaviour.

**Methods**

*Gene expression data*

Single-cell RNA sequencing data from the mouse brain was obtained from Zeisel et al (Zeisel et al., 2018) in Loom format. We used the dataset from the level 2 analysis that correspond to the olfactory neurons. The gene expression table represents the expression levels of 27,998 genes in 10,745 olfactory bulb cells. The gene expression level, which counts the number of expressed genes, was transformed into log2(count+1) before analysing further.

*Dimensionality reduction*: We screened for genes that have higher variability than expected by calculating a log-transformed Fano factor for each gene, as previously described (Li et al., 2017):

$$F(x) = log_{10}\left[\frac{\sigma^2(x)}{\mu(x)}\right],$$

where $\mu(x)$ and $\sigma^2(x)$ are the mean and the variance of the expression level across cells respectively. Then using the mean expression across different cells, we split the genes into 20 subsets and calculate the Z-score of the Fano factor within each subset:

$$Z(x) = \frac{\left[F(x) - mean\left(F(x)\right)\right]}{std[F(x)]},$$

where $\mathrm{mean}(\mathrm{F(x)})$ and $\mathrm{std[F(x)]}$ are the mean and the standard deviation of $\mathrm{F(x)}$ within the subset. The top 500 genes with the highest value of $\mathrm{Z(x)}$ were used to cluster the gene expression data. To visualise and cluster the gene expression data corresponding to individual cells in 2D space, we reduce the dimensionality using the principal component analysis (PCA) and t-distributed Stochastic Neighbor Embedding (tSNE; (van der Maaten and Hinton, 2008)). We used top 10 principal components to run tSNE with the following parameters: learning rate = 10, perplexity = 33. The result is shown in Fig. 1. Since many genes have similar expression patterns across different cells, in order to increase the power of PCA and tSNE, we extracted overdispersed genes i.e., the most informative genes.

*Clustering:* Using the 2-dimensional data above, hierarchical clustering algorithm HDBSCAN (Campello et al., 2013) was performed with the following parameters: min_clust_size = 5, min_pts = 13, which indicates which nearest neighbor to use for calculating the core-distances of each point. The cluster with the highest expression level of Tbx21 gene contained 101 cells. Within this group, clustering with HDBSCAN on tSNE space revealed 4 clusters. We then compared the *Cck* expression level across the clusters. We found that 18% (2 of 11) of cells from cluster #4 express *Cck* above the threshold = 3 (log2(count+1), while 64% (58 of 90) from clusters #1, #2 and #3 express *Cck* above the threshold, thus we defined the cluster #4 to be the putative MC cluster.

*Differential expression analysis and identification of molecular markers*: We used the Mann-Whitney U-test to find differently expressed genes. The test works under the assumption that the samples are independent. P-values were adjusted using the Benjamini-Hochberg procedure. We screened for significant genes, with the adjusted p value below the threshold = 0.05, where its median expression level in the MC cluster above the threshold = 3 in more than 50% of the cells. Of these, genes that are highly expressed in non-MC clusters were eliminated (cut-off of 10% of cells).

**Animals**

All animal experiments were approved by the animal experiment ethics committee of OIST Graduate University (protocol: 2018-201) and University of Tsukuba. ICR and C56BL/6J mice were purchased from Laboratories International, Inc. (Yokohama, Japan) for generation of transgenic mice, and C56BL/6J from Japan CLEA (Shizuoka, Japan) for subsequent breeding. Ai14 (Madisen et al., 2010) were from The Jackson Laboratory (Bar Harbor, USA), and Ra13-Cre was from the GENSAT project (Gong et al., 2003), via MMRRC (MBP, University of California, Davis). Mice of either sex were used in this study.

Generation of *Pkib-IRES-cre and Lbhd2-IRES-CreERT2 mice*

Vector construction for knock-in mouse production: The CRISPR target sequence (5'-ATAGCAGCTATGTATTCCTGGGG-3') was selected for integration of the IRES-Cre sequence just after the stop codon of *Pkib* and *Lbhd2*. The *pX330* plasmid, carrying both gRNA and Cas9 expression units, was a gift from Dr. Feng Zhang (Addgene plasmid 42230) (Cong et al., 2013). The oligo DNAs (Pkib-CRISPR F: 5'-caccATAGCAGCTATGTATTCCTG-3', and Pkib-CRISPR R : 5'-aaacCAGGAATACATAGCTGCTAT-3') were annealed and inserted into the entry site of *pX330* as described previously (Mizuno et al., 2014). This plasmid was designated as *pX330- Pkib*. The donor plasmid *pIRES-Cre-Pkib* contained the IRES sequence (Bochkov and Palmenberg, 2006), nuclear translocation signal (NLS)-Cre, and rabbit globin polyadenylation signal sequence. The 1.6-kb 5'-arm (from 1521 bp upstream to 64 bp downstream of *Pkib* stop codon) and the 2.0-kb 3'-arm (from 65 bp downstream to 2,038 bp downstream of *Pkib* stop codon) were cloned into this vector. DNA vectors (*pX330- Pkib* and *pIRES-Cre-Pkib*) were isolated with a FastGene Plasmid mini Kit (Nippon Genetics, Tokyo, Japan) and filtrated by MILLEX-GV 0.22 μm Filter unit (Merk Millipore, Darmstadt, Germany) for microinjection. Mice were kept in IVC cages under specific pathogen-free conditions in a room maintained at 23.5°C ± 2.5°C and 52.5% ± 12.5% relative humidity under a 14-h light:10-h dark cycle. Mice had free access to commercial chow (MF diet; Oriental Yeast Co., Ltd.., Tokyo, Japan) and filtered water.

*Microinjection and Genomic DNA analyses*

The pregnant mare serum gonadotropin (5 units) and the human chorionic gonadotropin (5 units) were intraperitoneally injected into female C57BL/6J mice with a 48-h interval and mated with male C57BL/6J mice. We collected zygotes from oviducts in mated females and a mixture of the *pX330- Pkib* (circular, 5 ng/μL) and *pIRES-Cre-Pkib* (circular, 10 ng/μL) plasmids was microinjected into 148 zygotes. Subsequently, surviving 137 injected zygotes were transferred into oviducts in pseudopregnant ICR females and 21 pups were obtained.

To confirm the knock-in mutation, the genomic DNA were purified from the tail samples using the PI-200 DNA extraction kit (Kurabo Industries LTD, Osaka, Japan) according to manufacturer's protocol. Genomic PCR was performed with KOD-Fx (TOYOBO, Osaka, Japan). The primers (Cre forward: 5'-TCTGAGCATACCTGGAAAATGCTTCTGT-3', and Pkib reverse: 5'-GTACCAGGAGCTCAAGACAACCTTACCC-3') were used for checking the 5' side correct knock-in and the primers (Pkib forward: 5'-CTATTTCACAGGTCCAGTTGCTGAAACC-3', and Cre reverse: 5'-ACAGAAGCATTTTCCAGGTATGCTCAGA-3') were used for checking the 3' side correct knock-in. We found 5 of 21 founders carried the designed knock-in mutation. In addition, we checked random integration of *pX330- Pkib* and *pIRES-Cre-Pkib* by PCR with ampicillin resistance gene detecting primer (Amp detection-F: 5'-TTGCCGGGAAGCTAGAGTAA-3', and Amp detection-R: 5'-TTTGCCTTCCTGTTTTTGCT-3') and no founder carried the random integration allele.

**Histology**

*In situ hybridisation:* ISH was performed using the RNAscope ISH system (ACDBio, Newark, CA, USA)(Wang et al., 2012).

*Brain extraction:* Whole brains were extracted and immediately placed in 4% PFA, dissolved in phosphate buffer (225.7 mM $NaH_2PO_4$, 774.0 mM $Na2HPO_4$, pH 7.4) at 4°C for 24 hours. Subsequently, the tissues were sunk in DEPC-treated 30% sucrose solution (~2 days), then embedded in OCT (4583, Sakura Finetech, Japan) in a cryomold (Peel-A-Way, Sigma-Aldrich) to be frozen in an ethanol/dry ice bath and stored at -80°C until use.

*Probe design*: ISH was carried out using RNAscope (ACDBio, Newark, CA, USA) and probes were produced by ACDBio to be compatible for the procedure. Sequence regions for the *Pkib* and *Ldhd2* probes were selected using the NCBI genetic database. For both probes, regions that were common to all splice variants of each gene were selected. The Pkib probe targeted the region 141-973 bp of the transcript XM_006512605.3. The *Ldhd2* probe targeted the region 138-715 bp of the transcript XM_006516048.1. The Tbx21 probe, which targets the region 893-2093 bp of the transcript NM_019507.2, was already commercially available (403331, ACDBio, USA).

*Hybridisation*: On the day of ISH, coronal olfactory bulb sections (20 µm) were cut on a cryostat (Leica CM3050S, Leica Biosystems) at -20°C, washed in RNAse-free PBS (Corning, Manassas, VA, USA), and immediately mounted on glass slides (Superfrost plus, Thermo Fisher Scientific, Waltham, USA). Slides were dried for 30 min at 60°C and post-fixed for 15 min in 4% PFA at 4°C. Slides then underwent *in situ* hybridisation using RNAscope reagents, according to manufacturer's protocols. Unless otherwise stated, all reagents were provided in the RNAscope kit (RNAScope Intro Pack 2.5 HD Reagent Kit Brown-Mm, Cat no. 322371). Briefly, slides were dehydrated through an ethanol series (75%, 90%, 100%, 100%, Sigma-Aldrich) and endogenous peroxidase activity blocked using provided hydrogen peroxide for 10 min at room temperature. Sections then underwent antigen retrieval by submersion into boiling (~98-102°C) 1X Target Retrieval Solution for 5 min and were rinsed in distilled water by submerging 5 times. Subsequently, slides were submerged into 100% ethanol 5 times and air dried. A barrier using an ImmEdge hydrophobic barrier pen was drawn around the sections and left overnight at room temperature to dry. On the following day, slides were treated with Protease Plus and incubated in an oven (HybEZ II System, ACDBio)

for 30 min, followed by a series of incubations in the same oven with provided solutions (AMP1-6) to amplify probes (AMP1&3: 30 min at 40°C; AMP2&4: 15 min at 40°C; AMP5: 30 min at room temperature; AMP6: 15 min at room temperature). After amplification, a DAB reaction was carried out (1:1 mixture of DAB-A and DAB-B solutions, Vector Labs, California, USA) for 10 min at room temperature. Slides were washed by submersion 5 times in 2 changes of distilled water.

*Counterstaining:* Olfactory bulb sections were immersed in Mayer's haematoxylin solution (MHS16, Sigma-Aldrich) for 10 mins. Excess stain was washed in distilled water and sections were differentiated by quick submersion in 0.2% ammonium hydroxide in distilled water, followed by washing for 5 minutes in distilled water. Slides were then dehydrated through a series of ethanol for 5 mins each, followed by two 5 min immersions in xylene. Slides were then covered with DPX mountant (06522, Sigma-Aldrich) for histology and left at room temperature to dry before imaging.

**Virus injection**

Three week-old, heterozygous *Lbhd2-IRES-CreERT2* mice were anaesthetised with isoflurane (IsoFlo, Zoetis Japan, Shibuya, Tokyo, Japan) and placed on a stereotaxic frame (Kopf, Tujunga, CA, USA). Carprofen (Rimadyl, Zoetis; s.c., 5mg/kg in saline) was injected subcutaneously for analgesia. The fur was trimmed, and the skin was disinfected with 10% iodine solution before incision. A craniotomy was made bilaterally over centre of the dorsal olfactory bulb (co-ordinates relative to Bregma: AP: 4.8 mm; ML: ± 0.8 mm). 100 nL of AAV1-pCAG-Flex-EGFP-WPRE (Addgene, Watertown, MA, USA) was injected from a pulled glass capillary tube (tip diameter approximately 10 um) at a depth 0.3 mm relative to the brain surface, at a rate of 2 nL every 5 s, using a Nanoject III injector (Drummond Scientific, Broomall, PA, USA). Following injection, the glass capillary was left in place for 1 minute and then slowly withdrawn. The surgical site was then sutured, and mice allowed to recover in a warmed chamber until fully awake, before being returned to their home cage. It is advisable that AAVs for conditional expression are tested before use, as they can exhibit off-target, "leak" expressions depending on the production protocol (Fischer et al., 2019), especially if not diluted enough.

**Tamoxifen administration**

Tamoxifen solution was dissolved at a concentration of 8 mg/mL in a solvent consisting of 5% ethanol and 95% corn oil (23-0320, Sigma-Aldrich), for once daily injections of 80 mg/kg (10 mL/kg injection volume). Tamoxifen powder (T5648, Sigma-Aldrich) was initially suspended in 100% ethanol and mixed using a vortex mixer to allow partial dissolution. Corn oil was subsequently added to make up solution to the final volume and the solution was heated up to 60°C with agitation on an orbital mixer in an oven, with periodic mixing on the vortex mixer. When fully dissolved (~30 min), the solution was cooled to room temperature, and mice were injected intraperitoneally using a 23G needle with care taken to avoid bubble formations. Injected mice were housed separately from untreated littermates. The mouse weights were monitored carefully throughout the injection period as well as 3 days after the final injection to ensure recovery. For a proof-of-principle P7 injections, 1 injection of 80 mg/kg was given using a 30G needle. A single-dose protocol was used to minimise disturbance to the pups and the nursing mother. Gloves were rubbed with the cage bedding prior to handling, and injected pups were returned to the cage with the mother.

**Two-photon functional imaging**

Cal-520 dextran (M.W. ~11,000, AAT Bioquest, Sunnyvale USA) was dissolved to 50 mg/mL in Ringer solution comprising (in mM): NaCl (135), KCl (5.4), HEPES (5), $MgCl_2$ (1), $CaCl_2$ (1.8). Cal-520 dextran solution was electroporated in the glomerular layer of the left OB of P42 *Lbhd2-CreERT2::Ai14* mice (tamoxifen dose = 3 x 80 mg/kg starting at P21), at a depth ~100 μm below the brain surface, under isoflurane anaesthesia. Parameters of electroporation were set according to the low intensity protocol described in (Hovis et al., 2010). Immediately after the electroporation, the craniotomy was sealed with an imaging window, and mice were anaesthetized with ketamine/xylazine (100 $mg.kg^{-1}$/20 $mg.kg^{-1}$, i.p.) and two-photon imaging of dye-loaded TCs and MCs were obtained with a custom two-photon microscope (INSS, South Chailey, UK) using 980 nm high-power laser (Insight DeepSee, SpectraPhysics) fitted with a water-immersion 25x objective (CFI75 Apo 25XC W 1300, Nikon, Japan) and resonance scanner (30 Hz frame rate; field of view was 256 x 256 μm, 512 x 512 pixels). MCs were those located ~ 300 μm below the brain surface (labeled = red fluorescent cells + green fluorescence, unlabelled = loaded cells without red fluorescence), while TCs were smaller cells located more superficially. Strongly fluorescent cells were excluded from analysis. 5 odours were presented in a randomized order using a custom-made, flow-dilution olfactometer (Koldaeva et al., 2019), at approximately 5% of the saturated vapour, while the total flow rate was 2 L/min. Odours used were ethyl butyrate, methyl tiglate, methyl butyrate, acetophenone and methyl salicylate. Inter-trial interval was 30 seconds during which lines were purged with pressurized air to minimise cross contamination. Due to bleaching and other time-dependent factors such as the depth of anaesthesia, typically, 3-4 presentations were given for each odour. For GCaMP6f imaging, *Lbhd2-CreERT2::Ai95D* mice were injected with tamoxifen intraperitoneally at P21 (1 x 160 mg/kg). After 2 weeks, the mice were surgically implanted with a cranial window over the left olfactory bulb, as well as a head plate, and allowed to recover. After 2 further weeks, they were anaesthetized with ketamine/xylazine, and head-fixed for imaging. Odours were presented in the manner described above for the electroporation experiment, but 6 odours were presented with the order randomly permuted. The additional odour was butyl acetate. The body temperatures of the mice were maintained at 36°C using a thermostat.

**Confocal Imaging**

Confocal images were acquired on a Zeiss LSM780 confocal microscope with a 10X objective (Zeiss, NA 0.45 Plan-Apochromat) for the whole brain sagittal sections, and 20X objective (Zeiss, NA 0.8 Plan-Apochromat) for the olfactory bulb. Using ZEN 2.3 software (Zeiss), images were taken at a resolution of 1024 × 1024 pixels for a field of view of 850.19 um x 850.19 um (10X) or 425.1 um x 425.1 um (20X objective). To enable comparison and quantification of viral injections, imaging conditions (resolution, gain, laser power, number of averages) were kept consistent. Sequential laser excitation was used to prevent fluorophore bleed-through. Images were taken throughout the whole rostro-caudal extent of viral spread using the 20× objective. For axonal projection analysis, images were acquired using a Leica SP8 confocal microscope using a 10X (Leica, NA 0.40 Plan-Apochromat) and a 40X (Leica, NA 1.3 Plan-Apochromat) objective. Images were taken at a resolution of 1024 x 1024 pixels per field of view (10X: 1163.64 x 1163.64 um; 40X: 290.91 x 290.91 um) at sequential excitation to prevent fluorophore bleed-trough.

**Image analysis**

*In situ hybridisation signal*: Images of DAB- and haematoxylin-stained olfactory bulb sections were obtained using a wide-field microscope with a 10X objective in RGB, so that the hematoxylin signal could be separated into the blue channel. The same acquisition settings were used for all sections (*Tbx21, Lbhd2 and Pkib* signals). Dorsal, ventral, medial and lateral portions of the olfactory bulb at 3 anterior-posterior locations were imaged so that all layers (nerve layer, glomerular layer, external plexiform layer, mitral cell layer and GCL) were captured. To extract the positions of the external plexiform layer boundaries, in ImageJ, a binary mask from the hematoxylin signal (blue) was obtained by setting a threshold and summed along the axis parallel to the olfactory bulb layers. Hybridisation signal (DAB; red channel) was converted into the binary mask, also by setting a single threshold across all conditions. Pixel co-ordinates were normalised such that the boundaries of external plexiform layer were set from 0 – 1, with mitral cell layer being 0. The density of the hybridisation signal was obtained by averaging the binary signal along the axis parallel to the olfactory bulb layers.

*Soma detection and quantification for olfactory bulb*: Confocal images (1024 x 1024 pixels corresponding to 425.1 um x 425.1 um) taken with a 20X objective were sampled at anterior, dorsal and ventral locations of the mid-sagittal plane for the tdTomato signal using the *Ai14* reporter line, using the DAPI channel to guide sampling, and 10 consecutive planes at a 100 μm interval for the virus injection experiment. Using only the red and green channel for tdTomato labeling and EGFP labelling, respectively, somata were detected manually in ImageJ using the ROI manager and their co-ordinates exported into Matlab, without the observer knowing the identity of the mouse. External plexiform layer boundaries were demarcated using only the DAPI signals from images, using a custom-written Matlab routine and the boundary co-ordinates were stored. The soma depths from above were normalised along the external plexiform layer using the boundary co-ordinates, such that the mitral cell layer was defined as 0, and the lower boundary of the GL as 1. One-way ANOVA was used to compare the means, using the *anova1* function in Matlab, and the *multcompare* function with the crucial value tested with Tukey's honest significant difference criterion for *post-hoc* multiple comparisons. Cells belonging to mitral cell layer were defined as those whose somata are positioned within 30% of the normalised external plexiform layer boundary from the MC layer. This corresponded, on average, to 43.6 μm, which is equivalent to the lengths of two MC somata (Nagayama et al., 2010). Thus, our measure takes into consideration the displaced MCs.

*Dendrite detection and quantification*: Images used were the same as those used to detect somata above. To emphasise signals originating from dendrites, which are thin processes, background signal was subtracted from the green or red channel using *Subtract Background* function in ImageJ, with the rolling ball radius set to 5 pixels. Binary masks were created with a single threshold value and the presence of the signal along the normalised external plexiform layer depth at each lateral position was averaged to obtain the density. The dendritic preference index was used to compare the dendritic signal in the upper external plexiform layer vs. lower external plexiform layer, as a proportion of the total dendritic signal detected, calculated as $(\text{Signal\_density}_{\text{upper\_EPL}} - \text{Signal\_density}_{\text{lower\_EPL}}) / (\text{Signal\_density}_{\text{upper\_EPL}} + \text{Signal\_density}_{\text{lower\_EPL}})$.

*Analysis of labelled MCs on a standardised coordinate*: Labelled MCs from coronal sections (1024 x 1024 pixels, 1.2 um per pixel) were automatically detected in ImageJ by converting the red fluorescence image

into binary masks by thresholding and converted into ROIs using the Analyze Particles function (100 – 600 pixels, circularity 0.1-1). The mitral cell layer was delineated using the DAPI channel in Matlab using the drawpolygon function. The line was interpolated, and labelled MCs were projected on the mitral cell layer coordinates. The centre of the olfactory bulb was calculated as the centre of the mitral cell layer coordinates. To pool data across mice, mitral cell layer coordinates were standardised such that it ran from $0 – 2\pi$ radians relative to the centre of the olfactory bulb.

*Whole brain somata detection*: Positions of somata labelled with tdTomato were automatically detected in the red channel of the stitched confocal images. To automatically detect the labelled somata, background fluorescence was subtracted using ImageJ's *Subtract Background* function (100 pixels), then further sharpened to accentuate the somata locally using ImageJ's *Unsharp* filter with the radius set to 14 pixels, and mask weight set to 0.6. Then a binary mask was obtained by setting a threshold and the *Analyze Particles* function was used to detect round objects (size = 70-600 pixels, circularity 0.1 - 1), and detected structures added to the ROI manager, and exported as a list. Using the DAPI signals in the blue channel, boundaries of each nucleus was manually drawn in Matlab using the *drawpolygon* function. Finally, for each anatomical region, all detected soma positions within the boundary were counted using the *inROI* function and normalised by the area to standardise the density of detected cells per $mm^2$. Distributions of labelled somata across strains were tested with 2-way ANOVA using Matlab's *anovan* function.

**Experimental Design and Statistical Analysis**

The Mann-Whitney U-test, t-test, Kolmogorov-Smirnov test, and 1-way- and 2-way-ANOVA were carried out using Matlab. Unless otherwise stated, t-tests were performed unpaired. Paired tests are described as "two-sample t-test" in the text. For *post-hoc* comparisons following significant ANOVA tests, the p-values are given in the following table for brevity of figure legends. Only the significant comparisons are listed due to the large number of pair-wise comparisons.

Table 1. *Details of post-hoc pair-wise statistical comparisons*

| **Figure** | **Test used** | **p-values** |
|---|---|---|
| Figure 1H | 1-way ANOVA followed by tukey-kramer multiple comparisons | P = 0.045 and 0.0086 for cluster 1 vs. cluster 2 and Cluster 2 vs. cluster 3, respectively for the null hypothesis that the two means do not differ. |
| Figure 2G | 1-way ANOVA followed by tukey-kramer multiple comparisons | P = 0.0008 for *Tbx21* vs. *Lbhd2*; 0.0035 for *Tbx21* vs. *Pkib,* respectively, for the null hypothesis that the two means do not differ. |

| | | |
|---|---|---|
| Figure 7E, left panel | 1-way ANOVA followed by tukey-kramer multiple comparisons | P = 0.012 for *Tbx21* vs. *Lbhd2* (1x80 mg/kg tamoxifen); 0.045 for *Tbx21* vs. *Lbhd2* (3x80 mg/kg tamoxifen); 0.008 for *Ra13* vs. *Lbhd2* (1x80 mg/kg tamoxifen); 0.029 for Ra13 vs. Lbhd2 (3x80 mg/kg tamoxifen), each for the null hypothesis that the two means do not differ. |
| Figure 7E, middle panel | 1-way ANOVA followed by tukey-kramer multiple comparisons | P = $8.8 \times 10^{-5}$ for *Tbx21* vs. *Lbhd2* (1x80 mg/kg tamoxifen); $1.5 \times 10^{-5}$ for *Tbx21* vs. *Lbhd2* (3x80 mg/kg tamoxifen); $6.5 \times 10^{-5}$ for *Ra13* vs. *Lbhd2* (1x80 mg/kg tamoxifen); $1.2 \times 10^{-5}$ for *Ra13* vs. *Lbhd2* (3x80 mg/kg tamoxifen), each for the null hypothesis that the two means do not differ. |
| Figure 7E, right panel | 1-way ANOVA followed by tukey-kramer multiple comparisons | P = $3.4 \times 10^{-5}$ for *Tbx21* vs. *Lbhd2* (1x80 mg/kg tamoxifen); $1.1 \times 10^{-4}$ for *Tbx21* vs. *Lbhd2* (3x80 mg/kg tamoxifen); $2.3 \times 10^{-4}$ for *Ra13* vs. *Lbhd2* (1x80 mg/kg tamoxifen); $8.0 \times 10^{-4}$ for *Ra13* vs. *Lbhd2* (3x80 mg/kg tamoxifen), each for the null hypothesis that the two means do not differ. |

Data will be available upon request. Lbhd2-CreERT2 has been donated to the Jackson Laboratory Repository (stock number 036054).

**Results**

In search of molecular markers, we sought to compare the gene expression patterns of MCs and TCs. This may reveal candidate markers, which are genes that are selectively enriched in the target cell-type of interest, in this case MCs, but not expressed in other cell types. This first requires a method to identify MCs and TCs in a gene expression data, and, second, distinguish their gene expression profiles from each other. Previous studies observed that *Tbx21*, a T-box type transcription factor, labels both MCs and TCs (Faedo et al., 2002; Mitsui et al., 2011; Haddad et al., 2013), while the neurotransmitter cholecystokinine (*Cck*) is more abundant in TCs (Seroogy et al., 1985; Economo et al., 2016). To verify these distributions in our hands, we crossed *Tbx21-Cre* and *Cck-IRES-Cre* lines (Taniguchi et al., 2011; Haddad et al., 2013) with the Rosa-CAG-LSL-tdTomato reporter line, *Ai14* (Madisen et al., 2012), for Cre-dependent expression of the red fluorescent protein, tdTomato. We confirm that Tbx21-driven expression labels cells in the mitral cell layer and the external plexiform layer where TCs are located, while *Cck*-driven expression labels a larger number of cells all over the olfactory bulb (Fig. 1A-C), especially those that extend more superficially in the glomerular layer and sporadically in the granule cell layer. Importantly, labeling coupled to *Cck* expression is less consistent in cells that occupy the mitral cell layer. These differential expression patterns between *Tbx21* and *Cck* may be used to distinguish MCs from TCs in gene expression data (Fig. 1B,C).

Identification of molecular markers by differential expression analyses requires a robust and large dataset, especially when distinguishing similar cell types, such as in the case of MCs and TCs. We turned to a public, large scale scRNA-seq dataset of the mouse brain (Zeisel et al., 2018). This contains data from approximately 0.5 million cells, 10,745 cells of which are from the olfactory bulb. We clustered the data based on the similarity of gene expression patterns. To achieve this efficiently, we identified the top 500 overdispersed genes out of 27,998 genes in the dataset (see Methods; Fig. 1D). Such genes are highly informative for determining genetic differences among the cells. Using this reduced dataset, we performed Principal Component Analysis (PCA), followed by t-distributed Stochastic Neighbor Embedding (tSNE) on the first 10 principal components to further reduce the dimensionality of the gene expression space to two. The combination of the two algorithms preserves both the global and local structures of the data (Kobak and Berens, 2019). To obtain clusters, hierarchical density-based special clustering algorithm (HDBSCAN (Campello et al., 2013)) was applied on the 2-dimensional tSNE space to cluster the data (see Methods). Within the olfactory bulb dataset, we found that 1,682 cells belong to *Cck*-positive clusters, while *Tbx21*-expressing cluster comprised 101 cells. Generally, expression patterns of *Cck* and *Tbx21* together mirror those of *Slc17a7* (VGlut1) and Slc17a6 (Vglut2), indicating that they are mainly glutamatergic populations (Fig. 1E,F), with the largest portion of glutamatergic, *Cck*-positive clusters residing outside of the Tbx21-positive cluster. Further, a small set of *Cck*-expressing neurons did not overlap with the *Slc17a7*-positive cluster (Fig. 1E,F). To identify a putative mitral cell cluster from the scRNA-seq data, we took advantage of the observation that MCs and TCs both express *Tbx21*, but *Cck* is more abundant among TCs. In the *Tbx21*-positive cluster, the second largest cluster (cluster 2, Fig. 1G) showed the lowest *Cck* expression level (Fig. 1H). We thus refer to this as the putative MC cluster, and refer to the remaining as TC cluster 1 (TC1).

An ideal molecular marker should be expressed abundantly and consistently in the cell type of interest, while having minimal expression levels in other cell types. To search for candidates with these properties, gene

expression patterns of putative MCs were compared against the rest of *Tbx21*-expressing neurons (TC1; Fig. 2A), as well as glutamatergic, *Cck*-positive clusters outside of the *Tbx21*-cluster (TC2; Fig. 2A). First, the Mann-Whitney U-test was used to screen genes that are differentially expressed, with p-values adjusted using the Benjamini-Hochberg procedure. This procedure identified several differentially expressed genes (Table 2), at the adjusted p = 0.05 level. Among these were *Calb2* (calbindin 2), *Ntng1* (netrin G1), *Ppm1j* (protein phosphatase 1J), *Rph3a* (rabphilin 3A), *Kcnq3* (voltage-gated potassium channel subfamily Q member 3), and *Chrna2* (cholinergic receptor nicotinic alpha 2). Of the differentially expressed genes, we focused on those that are present in the majority (>50%) of cells in the putative MC cluster, but in less than 10% of the cells outside of this cluster (Fig. 2B-H; Table 2). Only a small number of the differentially expressed genes fulfilled these criteria, and even fewer showed minimal expression levels outside of MCs, as judged by the OB-wide expression patterns (Fig 3A), as well as by the *in situ* hybridization data in the Allen Brain Atlas (Lein et al., 2007). Candidate genes that showed clear hybridization signals outside of the mitral cell layer were therefore not pursued further (Fig. 3B).

Based on the initial screening, *Pkib* (protein kinase inhibitor beta) and *Lbhd2* (LBH domain containing 2; Fig. 2C,D) genes fit the criteria for an MC marker. To confirm that these genes indeed are selectively expressed in MCs, we carried out *in-situ* hybridization for *Pkib* and *Lbhd2* (Fig. 2B-D) on olfactory bulb sections. Indeed, probes for *Pkib* and *Lbhd2* gave rise to monolayer-like signals at the lower boundary of the external plexiform layer, corresponding to the location of the mitral cell layer. For quantification, *Pkib* and *Lbhd2* signals were expressed as density (Methods) and plotted relative to the boundaries of the external plexiform layer. This revealed that *Pkib* and *Lbhd2* both label cells in the MC layer, with significant reduction in the superficial signals corresponding to TCs, especially compared to *Tbx21* (Fig. 2D; mean signal densities in the upper external plexiform layer: *Tbx21* = 0.39 $\pm$ 0.007; *Lbhd2*= 0.005$\pm$ 0.0002; *Pkib* =0.01$\pm$ 001, p = 0.0007, 1-way ANOVA, F = 17.9, degrees of freedom = 2). Hybridisation signal in the MCL was relatively uniform throughout the olfactory bulb (Fig. 2H), while residual expression patterns of *Pkib* and *Lbhd2* in non-MC cells differed somewhat, with faint signals in the glomerular layer and external plexiform layer for *Pkib* and *Lbhd2*, respectively. Thus, *Pkib* and *Lbhd2* are promising candidates for selectively labelling MCs. On the other hand, the same analysis failed to reveal clear molecular markers for sub-classes of TCs (Fig. 4).

Having identified candidate markers for MCs, we sought to test if Cre-recombinase expression from these loci would allow MC-specific labeling. Screening several public depositories, we found a Cre-driver line for *Lbhd2* under a synonymous gene symbol (A230065H16Rik) on GENSAT, a large repository of BAC-mediated transgenic mouse lines (Heintz, 2004; Gong et al., 2007). Since the two independent Cre-driver lines (*Ra31-Cre* vs. *Ra13-Cre*) show similar recombination patterns, we chose to analyse the line *Ra13-Cre*. As above, we crossed *Ra13-Cre* mice with *Ai14* reporter mice to analyse the pattern of Cre-mediated recombination in the brain (Fig. 5). At postnatal day 7 (P7), red fluorescence was highly selective, showing dense and restricted expression in the cells of the MC layer of the olfactory bulb (Fig. 5A-C; mean number of fluorescent TCs as a proportion of fluorescent cells in the mitral cell layer = 0.09 ± 0.04 for P7; p = 0.18, t-test for mean = 0, t-statistic = 2; n = 3 mice). Correspondingly, labelled dendrites were observed preferentially in the lower portion of the external plexiform layer (fluorescence signal density = 0.20 ± 0.03 for lower external plexiform layer vs. 0.10 ± 0.01 for upper external plexiform layer; p = 0.03, two-sample t-test for equal means, n = 3 mice each), consistent with MCs having dendrites that ramify in the deeper portion of the external plexiform layer. At this

developmental stage, red fluorescence was observed only sparsely in the rest of the brain, except for the lateral septum and the dorsomedial nucleus of the hypothalamus. However, in older mice, the residual recombination becomes widespread and is observed throughout the brain. In the olfactory bulb at this stage, while the labeling is still restricted to the projection neurons, a substantial number of tufted cells also become labelled (mean number of fluorescent cells in the upper external plexiform layer as a proportion of fluorescent cells in the mitral cell layer = 1.05 ± 0.08 for P21 and 1.33 ± 0.12 for P42). A Cre-driver line that we generated for the second marker candidate, *Pkib*, was deemed unsuitable for MC-specific labeling due to late-onset expression in MCs, as well as a wide-spread recombination in neurons other than MCs (Fig. 6).

The developmental accumulation described above makes *Ra13-Cre* unsuitable for investigating MCs in adult mice. However, the *in-situ* hybridization signal for *Lbhd2* mRNA indicates a clear preference for MCs in the adulthood. Therefore, it is possible that, when the recombination efficiency is calibrated appropriately, a more selective labelling of MCs may be feasible. To this end, we generated a new knock-in line (Fig. 7A) using CRISPR/Cas9, where the inducible Cre-recombinase, Cre-*ERT2* (Feil et al., 1997), is inserted into the 3'UTR of the *Lbhd2* gene (the target sequence: 5'-ACCAAGAGGACCTCCAT-3'; Fig. 7A).

To test if selective labelling is maintained beyond P7 in the new, inducible Cre-driver line, we injected tamoxifen intraperitoneally at P21 in *Lbhd2-CreERT2::Ai14* mice, and analysed the distribution of red fluorescence 3 weeks post injection to assess the recombination pattern (Fig. 7B-E, Fig. 8A). At the lowest dose tested (one injection of 80 mg/kg), the labeling was sparse (average density of labelled MCs = 5.7 $\pm$ 0.9 cells per mm), but 83.7 $\pm$ 3.7% of labelled somata were located in the mitral cell layer (Fig. 7C,D). Other labelled cells were mostly TCs, save for sporadic labeling in granule cells, which constituted about 1% of the labelled cells. When the dose was increased to three intraperitoneal injections of tamoxifen (at 80 mg/kg *per diem*, over three days), denser labeling was achieved (mean density = 10 $\pm$ 4 cells per mm; 78.0 $\pm$ 11.0% of labelled somata were in MCL) while maintaining specificity, indicating that the tamoxifen dose can be calibrated to titrate the specificity and density of labeling. Compared to the patterns of recombination observed with existing lines, namely *Tbx21-Cre* and *Ra13-Cre* mice, overall, the new line achieves a labeling that is substantially more selective for MCs, as measured by the positions of somata ($p = 0.016$, $F = 6.01$, 1-way ANOVA; n = 3 mice for *Tbx21-Cre* and *Ra13-Cre*, 4 mice for *Lbhd2-IRES-CreERT2*) and dendrites ($p = 2.99 \times 10^{-6}$, $F = 59.31$, 1-way ANOVA; n = 3 mice for *Tbx21-Cre* and *Ra13-Cre*, 4 mice for *Lbhd2-IRES-CreERT2*). Consistent with the recombination pattern observed with the Ra13-Cre line, tamoxifen injection at P7 also resulted in a mitral cell-specific labeling (Fig. 8B). To test if AAV-mediated conditional labeling is possible, AAV1-pCAG-Flex-EGFP-WPRE (100 nL) was stereotaxically injected into the dorsal olfactory bulb at a depth of 300 μm below the brain surface in P21 *Lbhd2-CreERT2::Ai14* mice. Tamoxifen injections (3 x 80mg/kg, i.p.) overlapped such that the first of the three injections occurred immediately after the AAV injection. Three weeks later, labeling pattern was analysed, which showed predominantly MC-selective labelling similar to the pattern obtained with the *Ai14* reporter line (Fig. 8C).

Having achieved MC-selective labeling with the *Lbhd2-CreERT2* line, we wished to further characterize the properties of the labelled cells in the olfactory bulb, as well as the distribution of labelled fibres in the olfactory cortices (Fig. 9). Specifically, we wished to assess if the labelled MCs are present uniformly in all domains of

the olfactory bulb. To this end, confocal images from coronal sections from anterior, middle and caudal levels of the olfactory bulb from *Lbhd2-CreERT2::Ai14* mice were analysed. This revealed consistent mitral cell layer labeling in all regions of the olfactory bulb, except for the most anterior level, which tended to show a sparser labeling on the medial side (Fig. 9B-D), though this was not statistically significant ($p = 0.56$, two-way ANOVA; n = 3 mice). In terms of the projection patterns of labelled fibres in the olfactory cortices, we detected red fluorescent fibres as fascicles throughout the antero-caudal extent of the lateral olfactory tract (Fig. 9A,B), as well as thin fibers with bouton-like structures in the molecular layers of olfactory cortices, including in the anterior olfactory nucleus, olfactory tubercle, and the anterior and posterior piriform cortices (Figure 9E-G).

In addition to the anatomical traits, to assess the labelled cells functionally, we loaded a synthetic calcium indicator, Cal-520 dextran by electroporation (Fig. 10A) using a low intensity protocol (Hovis et al., 2010). Using two-photon microscopy in mice anaesthetized with ketamine and xylazine, odour response properties of labelled MCs vs. superficially located TCs were compared (Fig. 10A,B). As above, we used 42 day-old *Lbhd2-CreERT2::Ai14* mice, where recombination was induced with tamoxifen (3 x 80 mg/kg) at P21. Consistent with previous reports (Nagayama et al., 2010; Burton and Urban, 2014; Ackels et al., 2020; Eiting and Wachowiak, 2020), odours excited TCs more than labeled or unlabeled MCs (Fig. 10C,D). No obvious difference was observed between labeled and unlabeled MCs. However, the lack of convincing responses raises some questions about the identity of labelled cells. Localised loading of dyes by electroporation allows a direct comparison of TCs and MCs belonging to the same glomerulus, but the low-yield and the low sensitivity of the indicator are disadvantageous, especially when responses are sparse. To address this, we expressed GCaMP6f conditionally by crossing the Lbhd2-CreERT2 line with the Ai95D line (Madisen et al., 2015), with tamoxifen injection at P21. Two weeks later, the injected mice were implanted with a cranial window over the left olfactory bulb, and after two further weeks, the olfactory bulb was imaged with a two-photon microscope under ketamine/xylazine anaesthesia. On average, 5-6 fluorescent cells were visible in a given field of view (256 x 256 μm) at a depth ~ 300 μm below the brain surface (Fig. 10E). This time, a fraction of cell-odour pairs (22.2%; n = 270 cell-odour pairs, 45 cells; 4 mice) exhibited robust fluorescence increases locked to odour presentations (Fig. 10F), even though the majority of cells did not show detectable responses to any of the 6 odours presented (Fig. 10G). Overall, the results here indicate that the new inducible Cre-driver line, *Lbhd2-CreERT2*, achieves a highly specific labeling of functional MCs in the olfactory bulb.

Finally, we examined the recombination pattern in the brain at large, beyond the olfactory bulb. To assess this, we analysed the distribution of labelled somata in the anterior olfactory nucleus, olfactory tubercle, anterior and posterior piriform cortex, and tenia tacta, as well as other, commonly studied regions, including the thalamus, cerebellum, hippocampus and cerebral cortex. In the *Lbhd2-CreERT2* mice, for both doses of tamoxifen tested, consistent labeling was observed unexpectedly in a small number of nuclei, including the ventromedial nucleus of the hypothalamus and the lateral septum (Fig. 11- 12). Compared to the *Ra13-Cre* driver line, the olfactory cortices were devoid of fluorescent cells (Figure 7C; no labelled cells were detected for aPCx, pPCx, AON and OT in *Lbhd2- CreERT2::Ai14* mice; in *Ra13*::*Ai14* mice, mean density of labelled cells = 91.2, 38.5, 490.2, 818.0 labelled cells per $mm^2$ for aPCx, pPCx, AON and OT, respectively; $p = 1.03 \times 10^{-38}$, $F = 295.04$, 2-way ANOVA, with mean densities for *Lbhd2- CreERT2* groups were significantly different from *Ra13-Cre*; n = 3 mice per group). Thus, the results indicate that the labelling is, overall, relatively specific to MCs in

545 the whole brain, suggesting that the new inducible Cre-driver line may be suitable for a variety of studies to
546 investigate olfactory processing.

## Discussion

A wide variety of neuron types that exist in the sensory systems are thought to reflect diverse components for information processing in the brain (Masland, 2004; Luo et al., 2018). Availability of Cre-driver lines have led to a multitude of fundamental insights into unique, cell-type specific contributions to sensory processing and perception (Münch et al., 2009; Dhande et al., 2013; Cruz-Martín et al., 2014; Takahashi et al., 2020). Recent progress in the acquisition, analyses, and applications of large-scale gene expression data have allowed efficient analysis of the differences between cell-types of interest (Birnbaum, 2018; Luo et al., 2018). In this study, we used a publicly available gene expression dataset to discover candidate molecular markers for the key second-order cells of the olfactory system, MCs, which we validated with histology, and finally with new Cre-driver lines generated by CRISPR/Cas9-mediated gene editing. We report that one driver line in particular provides a substantial improvement in the ability to selectively label MCs.

Among the several candidates identified from our differential expression analysis, we found *Lbhd2* to be the most promising. Specifically, at postnatal day 7, the recombination pattern for the non-inducible, *Ra13-Cre::Ai14* is restricted mainly to MCs in the olfactory bulb. This pattern is consistent with the description on the GENSAT expression database (Gong et al., 2007). Since TCs are already present and located superficially in the external plexiform layer at this stage of development (Mizuguchi et al., 2012), this pattern likely reflects genuine MC specificity in neonatal mice. Despite an increase in the sporadic *Lbhd2*-driven labelling of TCs and other regions of the brain at later stages, the preferential expression in MCs over TCs that persists in adulthood can be utilized to our advantage. Thus, with our new inducible Cre-driver line, the expression can be targeted selectively to MCs even in the adulthood. It is notable that, despite the fact that many genes were differentially expressed across the two cell types, markers suitable as genetic tools are harder to identify, especially when selective expression is required across developmental stages. This difficulty may partly be due to the similarity between MCs and TCs, and that cell types are often defined by a combination of genes, rather than single genes (Luo et al., 2018).

In the olfactory bulb, labelled MCs were present in most domains of the olfactory bulb, except for a small patch on the medial, anterior olfactory bulb that showed a curious lack of labeling. Whether or not these correspond to subclasses of MCs, for example those that differ in the glomerular association (Li et al., 2017), or cortical projection patterns (Zeppilli et al., 2020), will be intriguing for future investigation. Outside of the olfactory bulb, labeled somata were sparse if not absent, especially in the areas that MCs target, including in the anterior olfactory nucleus, olfactory tubercle, and the anterior and posterior piriform cortices. This makes the *Lbhd2-CreERT2* line suitable for investigating the downstream, decoding mechanisms of mitral-specific activity in all these areas, and also when imaging from boutons of MCs (Pashkovski et al., 2020). Beyond these areas, however, we observed a small number of specific regions that showed the presence of labelled somata. The areas include the lateral septum, ventromedial nucleus of the hypothalamus, and the medial amygdala, even at the lowest dose of tamoxifen used. Thus, future studies using this line need to take this into account when interpreting data, in particular for investigating innate, social behavior, which involve these areas (Stowers and Liberles, 2016). However, the fact that only a subset of the nuclei in the pathways are labelled may make this line unexpectedly useful for investigating mechanisms of social behaviour.

This study was aided by publicly accessible data, speeding up discovery. One limitation, if any, in using this dataset for this study may have been the data size, where only a small fraction of olfactory bulb cells expressed *Tbx21*, and even fewer belonged to the putative MC cluster. The relatively small MC cluster size may partly be biological. Of the neurons present in the OB, approximately 80% are GABAergic. Further, glutamatergic neurons comprise heterogenous groups, including those that lack lateral dendrites (Hayar et al., 2004; Antal et al., 2006). Thus, MCs comprise only a small proportion (~1%) of OB neurons (Burton, 2017; Schwarz et al., 2018). Our histology indicates that superficially located, *Tbx21*-expressing cells are located below the glomerular layer, unlike the *Cck*-expressing population that includes a dense population located more superficially. It should also be noted that a large proportion of glutamatergic and *Cck*-expressing cells were found outside of the *Tbx21*-positive cluster. Some of this latter group may correspond to external tufted cells, which are glutamatergic but lack lateral dendrites (Macrides and Schneider, 1982). It is possible that protocols used to obtain the scRNA-seq data may have been inadvertently biased against large cells with prominent dendrites, such as the filtering step involving a pore size of 30 um (Zeisel et al., 2018).

Despite the need for tamoxifen, this new method for labeling MCs has several advantages over the existing methods. Currently, MC labeling and manipulations are achieved predominantly by depth, birthdate, or retrograde viral expression utilizing the differential projection targets of MCs vs TCs (Haberly and Price, 1977; Imamura et al., 2011; Rothermel et al., 2013; Economo et al., 2016). While this can indeed bias expression patterns, the overlap in somatic and dendritic locations (Schwarz et al., 2018), as well as projection targets (Haberly and Price, 1977; Igarashi et al., 2012) means that it is not trivial to achieve a highly selective labeling. In contrast, our transgenic mouse line described here allows for reproducible and selective labeling of MCs over TCs, with the added advantage that labelled MCs are located throughout the olfactory bulb. Even in imaging applications that can distinguish the cell type based on the soma depth, with the new driver line, it will be possible to investigate the physiology of subcellular compartments, such as the long lateral dendrites, without the need to painstakingly trace back the structures to somata for cell-type identification. Similarly, investigations of downstream decoding mechanisms, such as one involving precise optogenetic activations of olfactory bulb projections using patterned light stimuli (Chong et al., 2020), may now be done in a cell-type specific manner. Thus, our new tool may bring us closer to understanding how parallel olfactory processing contributes to mechanisms of sensory perception and, ultimately, behaviour.

**Acknowledgement**

We would like to thank OIST's Imaging section, sequencing team, and AAALAC-accredited animal facility staff for assistance, and Bernd Kuhn, Sander Lindeman and Gonzalo Otazu for comments on the manuscript. This work was supported by the OIST Graduate University.

**Author contributions**

HM and IF conceived the project; AK, CZ, YPH and IF designed the experiments with help from HM and JKR; CZ, YPH, TS, JKR & IF carried out the experiments; SM, FS and ST generated the transgenic mice; AK and IF analysed the data with help from HM; and IF wrote the manuscript with inputs from all authors.

## Figures

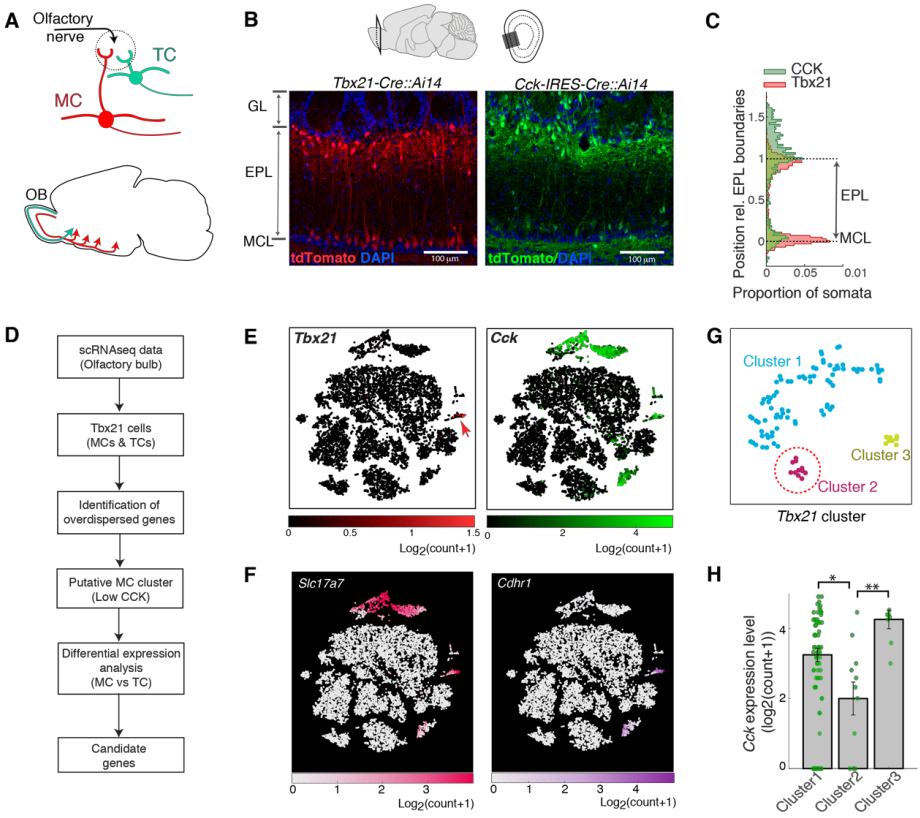


**Figure 1**: *Strategy for identifying mitral-cell specific markers from scRNA-seq data*

(**A**) Schematic showing major anatomical differences between the two cell types; MCs (red) are located deeper in the olfactory bulb (OB) layers, and project widely in olfactory cortices. TCs (green) are smaller, superficially located principal neurons that project to anterior portions of the olfactory cortex. (**B**) *Tbx21* and *Cck* expression patterns in the main olfactory bulb; example images showing tdTomato expression patterns in *Tbx21*-Cre::Ai14 mouse (red) and Cck-IRES-Cre::Ai14 mouse (green). Scale bar = 100 µm. GL = glomerular layer, EPL = external plexiform layer, MCL = MC layer. (**C**) Soma positions of tdTomato-expressing cells relative to the EPL boundaries, for the images shown in **B**. EPL depth was normalized so that it ranged from 0 to 1, with the lower boundary (MCL) corresponding to 0. (**D**) Schematic of workflow; Putative mitral cluster from scRNA-seq data is identified by the observation that MCs and TCs both express *Tbx21*, but *Cck* is more abundant among TCs. Once putative MC and TC clusters were identified, differential expression analysis was carried out to identify genes that are selectively expressed in MCs. (**E**) OB cells plotted in tSNE coordinates, with *Tbx21* and *Cck* expression levels (left and right panels, respectively) indicated with colour maps shown below. (**F**) Expression levels of common markers for projection neurons of the OB; VGlut1 (*Slc17a7*) and *Cdhr1*. (**G**) *Tbx21*-positive cluster was further analysed and the sub-clustered and displayed in new tSNE coordinates. (**H**) *Cck* expression levels for the sub-clusters in (**E**). Cluster 2 has the lowest level and is inferred to be the putative MC cluster (red dotted line in **E**). Stars indicate a statistical significance at the 0.05 level (*) and 0.01 level (**). For details, see the Experimental Design and Statistical Analysis section.

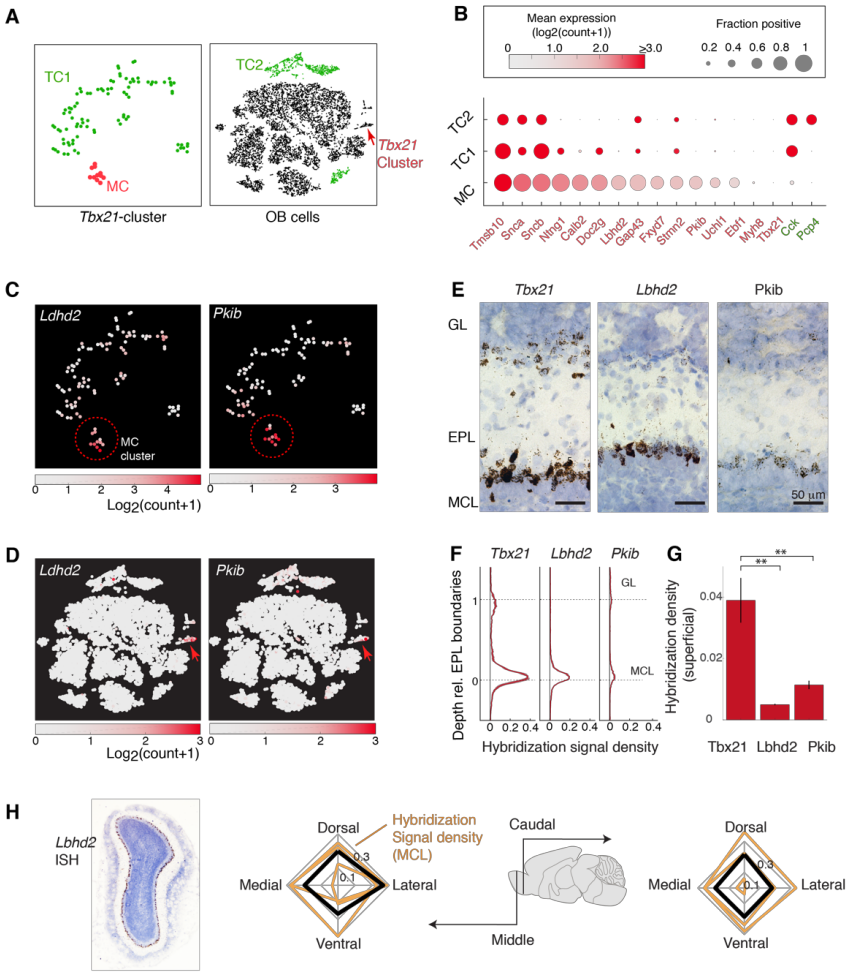


**Figure 2**: *Differential gene expression analysis reveals candidate marker genes for MCs*
(**A**) Cluster grouping used for differential gene expression analysis to distinguish TCs from MCs. *Tbx21* expressing cells (left) constitute the MC cluster (red) and TC1 cluster (green), which is identical to the combined clusters 1 and 3 shown in Fig. 1G. The olfactory bulb (OB)-wide dataset (right) contains the TC2 cluster (green) which is equivalent to the *Cck*-rich clusters shown in Fig. 1E without the *Tbx21*-rich clusters. (**B**) Genes that are significantly enriched in MCs (red), and TC clusters (green). The size of data points indicates the consistency of expression, measured as the fraction of cells in the cluster that express the gene. Mean expression level (log2(count+1)) is color-coded as shown in the colormap above. (**C**) Expression levels of two candidate genes, *Pkib* and *Lbhd2*, with the corresponding colormaps, superimposed on the 3-sub clusters of the *Tbx21*-rich cluster (same tSNE coordinate as Figure 1G) and (**D**) the whole OB data. Red arrow points to the *Tbx21*-cluster. (**E**) Example *in-situ* hybridization signals revealed by DAB staining, for *Tbx21* (left), *Lbhd2* (middle) and *Pkib* (right) for the MOB layers indicated. Scale bar = 50 μm. (**F**) *In-situ* hybridization signal density relative to the external plexiform layer boundary (0 – 1); hybridization signal was thresholded, and the proportion of pixels above the

threshold for each normalized external plexiform layer depth was expressed as density. (**G**) Summary of hybridization signals in the superficial locations (depth upper half of external plexiform layer). N = 3 mice, with samples from dorsal, ventral, medial and lateral locations at middle and caudal levels of the antero-caudal axis. (**H**) Quantification of regional variation; average hybridization signal density from the MCL (right) for dorsal, ventral, medial, and lateral samples taken from middle plane (bottom plot) and caudal plane (top plot) of the antero-posterior axis. Orange lines correspond to data from individual mice, and black lines show the average across the 3 mice.

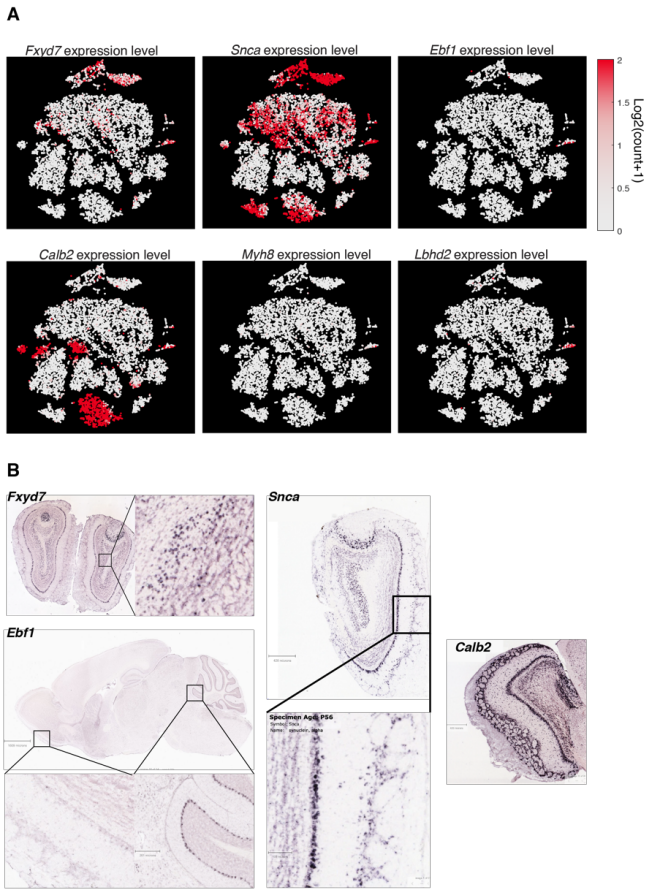


**Figure 3:** OB-wide tSNE data and *Allen Brain Atlas ISH data used to screen candidate MC markers that were not analysed further.*
Differential expression analysis indicates that *Fxyd7*, *Ebf1*, *Snca*, *Calb2*, and *Myh8* are significantly enriched in MCs relative to TCs. (**A**) To screen candidates, the expression pattern (colormap) in the whole OB data were analysed. The same tSNE coordinates as in Fig. 1E,F are used, with *Lbhd2* expression pattern shown for comparison. (**B**) Further, the ISH database of the Allen Brain Atlas was used to assess the spatial expression patterns. *Fxyd7* seems to be expressed by neurons deep in the granule cell layer as well as superficial cells. *Snca* is expressed by some superficially located neurons as well as some neurons of the anterior olfactory nucleus. *Ebf1* is hardly detectable in the OB even though it is present in the Purkinje cell layer of the cerebellum. Dense *Calb2* hybridisation signal is visible in the glomerular layer, external plexiform layer, mitral cell layer, as well as the granule cell layer. *Myh8* signal was not described in the ISH database but it is a marker for somatostatin positive cells in the subventricular zone (Lim et al., 2018), which is the source of SST-positive interneurons of olfactory cortices. The expression data in (**A**) shows low levels of Myh8 expression in many neurons outside of the Vglut1- and 2-positive clusters. Image credit: Allen Institute.

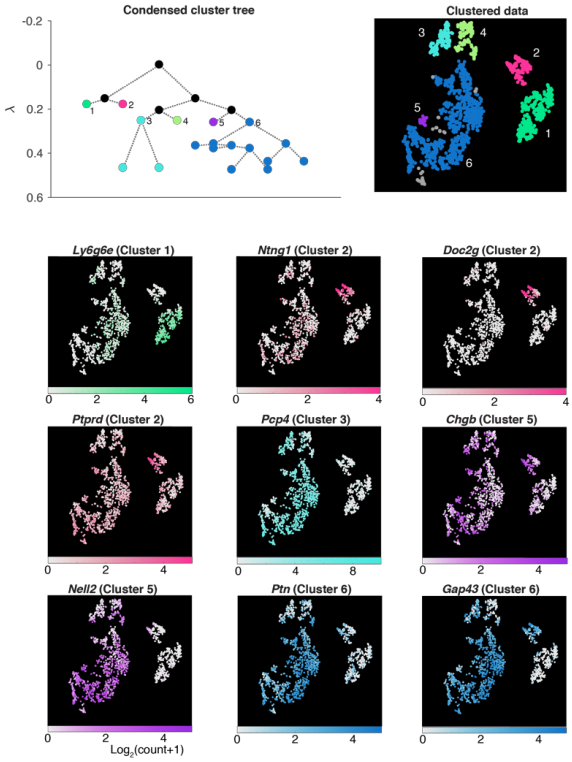


**Figure 4**: *Sub-clustering analysis of the Cck-expressing cluster*
The Cck-expressing population from the OB dataset was further analysed to reveal sub-clusters. For each sub-cluster, candidate marker genes were identified by differential gene expression analysis, where expression patterns from a cluster of interest was compared against all other clusters combined. The expression patterns for each candidate marker, and in which sub-cluster the gene is enriched (in brackets), are shown for all cells in the Cck-positive population, with corresponding colormaps. While the Doc2g gene selectively labels the sub-cluster 2 in the TC-dataset, it is a gene that is also abundantly expressed by MCs (Fig. 2).

710

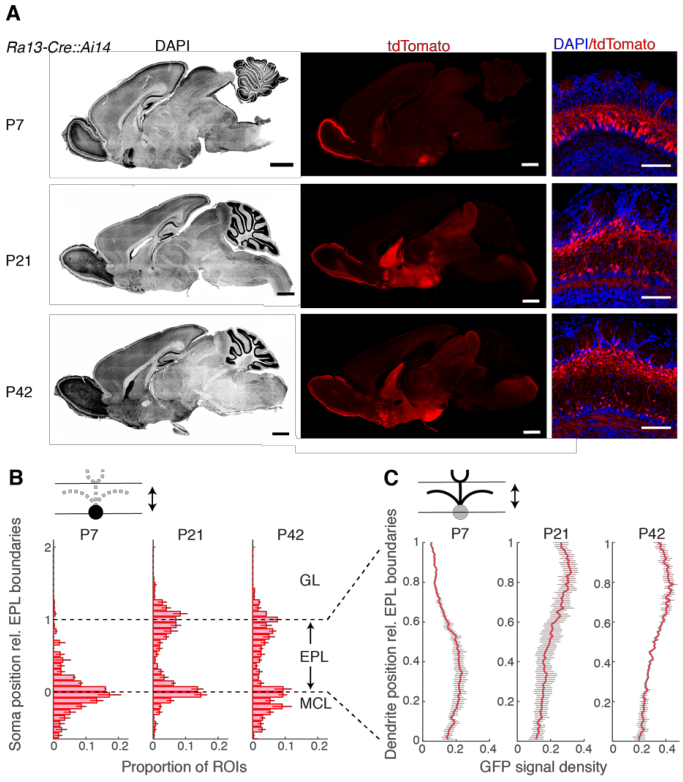


711
712 **Figure 5**: The *Ra13-Cre::Ai14 line reveals a developmental accumulation of recombination patterns outside of MCs*
713 (**A**) Sagittal brain sections from example P7 (top row), P21 (middle row) and P42 (bottom row) mice, showing DAPI
714 signal (left column; pseudo-coloured in grey scale), corresponding tdTomato (middle column) and merged signals
715 for OB (right column). Scale bar = 1 mm for the whole sagittal view, and 100 μm for OB. (**B**) Distribution of somata
716 positions with respect to the external plexiform layer boundaries. N = 3 mice (average of measurements from
717 anterior, ventral and dorsal parts for each animal). (**C**) Distribution of labelled dendrites with respect to the external
718 plexiform layer boundaries.
719

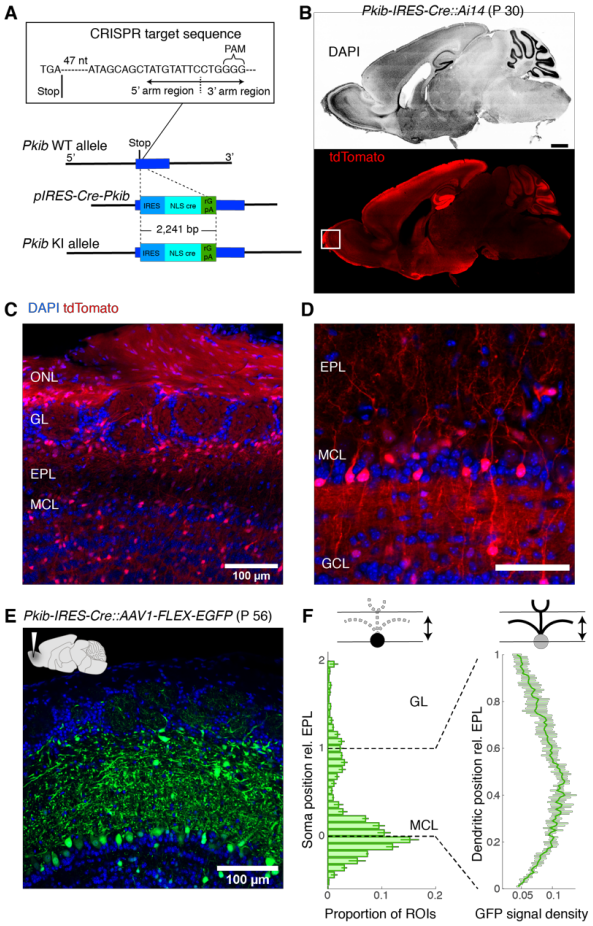


**Figure 6:** *Pkib-IRES-Cre* labels a wide variety of non-MC neurons, with late onset labeling in MCs

(A) Strategy for CRISPR/Cas9 – mediated generation of the *Pkib-IRES-Cre* transgenic mouse. The CRISPR-target sequence (inset) was just after the stop codon of the Pkib gene. Construct included sequences for IRES, Cre-recombinase with a nuclear localization signal, and rGpA. (B) Cre-mediated recombination pattern in a 30-day old *Pkib-IRES-Cre::Ai14* mouse. Structures visible in this sagittal plane is revealed by DAPI (top panel), and the corresponding pattern of recombination revealed by tdTomato signal. Scale bar = 0.5 mm. (**C**) tdTomato expression pattern relative to the OB layers from the same animal. ONL = olfactory nerve layer; GL = glomerular layer; EPL = external plexiform layer; MCL = mitral cell layer. Note the dense labeling of the ONL. (**D**) A higher magnification of image in **C**. Signals in the MCL are faint or lacking at this developmental stage. Scale bar = 0.1 mm. (E) A confocal image showing the EGFP expression pattern two weeks after an injection of AAV1-flex-EGFP into the MOB in a 42-day old *Pkib-IRES-Cre* mouse. (F) Summary of soma location (left) and dendritic signal density (right) relative to the EPL boundaries. Note the heavy presence of somata outside of the MCL and dendrites in the upper portion of the EPL.

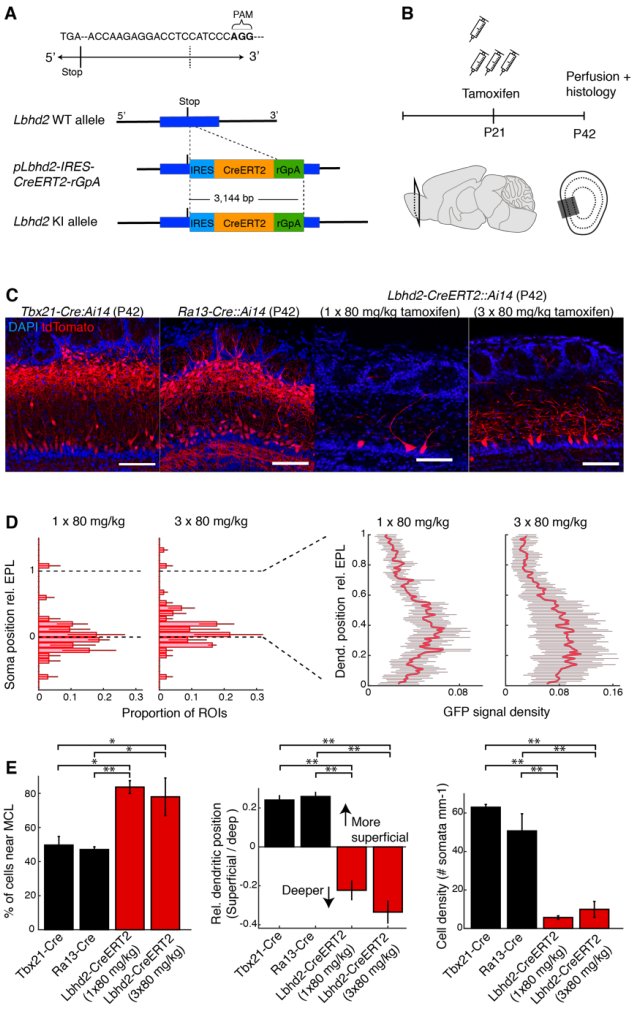


**Figure 7**: *Lbhd2-CreERT2 line achieves MC-specific labeling in the olfactory bulb even in the adulthood*

(**A**) Constructs for CRISPR/Cas9-mediated knock-in line. IRES-CreERT2 cassette was targeted to a region immediately following the stop codon of the Lbhd2 gene. (**B**) Schematic of the tamoxifen injection protocol: tamoxifen was injected intraperitoneally at P21, and the recombination pattern in the OB was examined 3 weeks later. Cohorts of mice received injection for either one or three days at 80 mg/kg *per diem*. (**C**) Example recombination patterns. From left: *Tbx21-Cre::Ai14*, *Ra13-Cre::Ai14*, *Lbhd2-CreERT2::Ai14* (one injection) and *Lbhd2-CreERT2::Ai14* (three injections). Scale bar = 100 μm. (**D**) Summary of labelled structures at P42 for the corresponding mouse lines, showing the proportion of cells in the mitral cell layer relative to all labelled cells (left), comparison of labelled dendrites in the superficial vs. deep portions of the external plexiform layer (middle), and density of labelled somata in the mitral cell layer (right). (**E**) Comparison of labeling patterns between *Tbx21-Cre::Ai14*, *Ra13-Cre::Ai14* and *Lbhd2-CreERT2::Ai14* lines. Left: Labelled cells in the mitral cell layer as a percentage of total number of labelled cells. Middle: tdTomato signal density in the upper half of EPL subtracted by the signal density in the lower half of

EPL. Right: Number of labelled cells detected per mm of MCL. N = 3 mice per transgenic line for all plots. Mean and s.e.m. shown. Stars indicate a statistical significance at the 0.05 level (*) and 0.01 level (**). For details, see the Experimental Design and Statistical Analysis section.

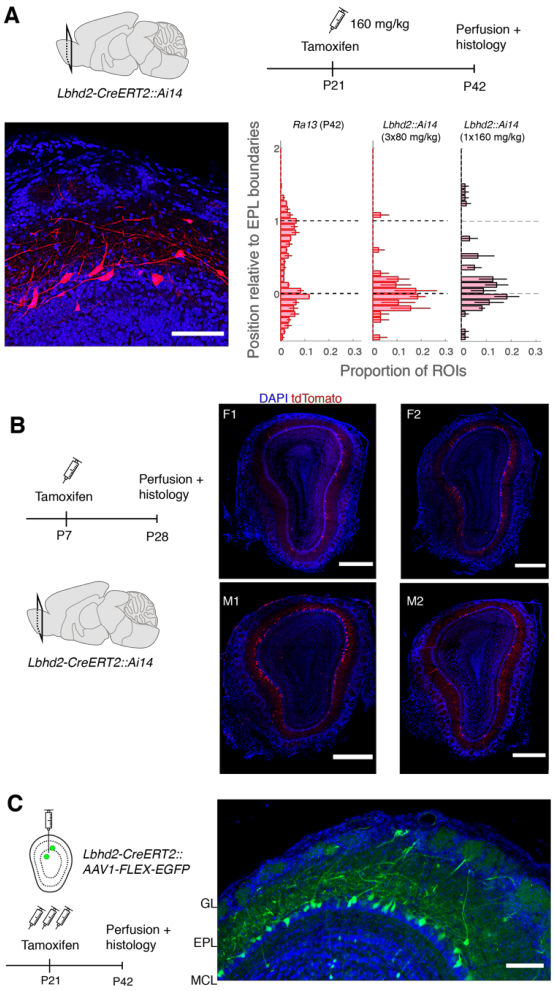


**Figure 8**: *Further characterization of tamoxifen-dependent recombination*.
(**A**) Recombination pattern after 1 x 160 mg/kg at P21, with tdTomato analysed at P42. Scale bar = 0.1 mm. Bottom right: summary of labelled soma positions relative to the EPL layers in comparison to Ra13-Cre::Ai14 and Lbhd2-CreERT2::Ai14 (3 x 80 mg/kg). N = 3 mice. (**B**) Recombination pattern following tamoxifen-injection at P7. Lbhd2-CreERT2::Ai14 pups at post-natal day 7 were injected with a lowest dose tamoxifen (80 mg/kg intraperitoneally, once). Right: recombination patterns from 2 females (F) and 2 males (M), as indicated. Scale bar = 0.5 mm. (**C**) Tamoxifen-induced recombination with AAV-mediated expression. Tamoxifen (3 x 80 mg/kg) was administered intraperitoneally starting on the day of AAV (AAV1-flex-EGFP) injection in the dorsal OB and EGFP expression analysed three weeks later. Note that AAVs for conditional expression can exhibit Cre-independent, "leak expression" depending on the production protocol, (Fischer et al., 2019) or if not diluted enough.

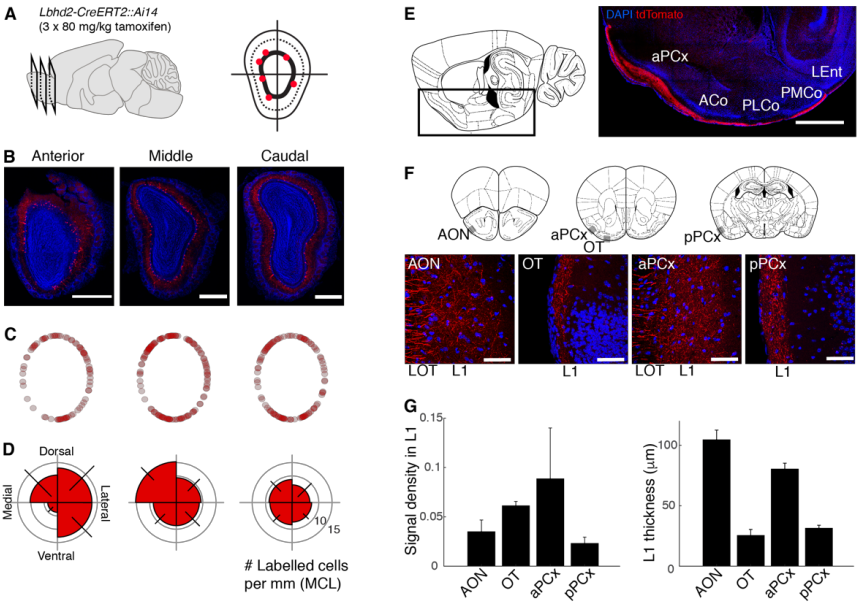


**Figure 9**: *Properties of labelled MCs: OB domain-dependent variations and axon projection patterns*
(**A-D**) Distribution of labelled MCs in the OB. (**A**) Schematic of analysis approach: positions of labelled MCs (red dots) were analysed for anterior, middle and caudal levels of the OB of Lbhd2-CreERT2::Ai14 mice (tamoxifen dose = 3 x 80 mg/kg). Angular positions were measured relative to the centre of the olfactory bulb. (**B**) Coronal OB images at each antero-posterior level from an example animal. Scale bar = 0.5 mm. (**C**) Positions of labelled MCs from all animals (one dot = one labelled MC), projected on a standardized mitral cell layer position (see Methods). N = 3 mice. (**D**) Polar histograms showing the number of labelled MCs per mm of mitral cell layer for each quadrant. Error bar = s.e.m. (**E-F**) Projection patterns of labelled fibres. (**E**) Image of a sagittal brain section (right) at the medio-lateral plane indicated in the illustration (left), with the imaged location marked by the black outline, showing tdTomato signal present in the lateral olfactory tract (LOT) and the molecular layer for the entire antero-caudal extent of the anterior piriform cortex (aPCx), anterior cortical amygdaloid nucleus (ACo), posterolateral cortical amygdaloid nucleus (PLCo), and posteromedial cortical amygdaloid nucleus (PMCo). Scale bar = 1 mm. (**F**) High magnification (40X objective) of coronal sections taken at the planes shown in illustrations (top). Grey boxes indicate approximate location of images below. Labelled fibres appear as fascicles in the LOT, while thinner, densely present labelled fibres are visible in the superficial, molecular layer (L1) for the anterior olfactory nucleus (AON), olfactory tubercle (OT), and the anterior and posterior piriform cortices (aPCx and pPCx, respectively). Scale bar = 50 μm. (**G**) Summary quantification of signal density in the molecular layer for the 4 regions (left), and the thickness of the labelled L1 for the corresponding regions (right). N = 3 mice, one image plane each.

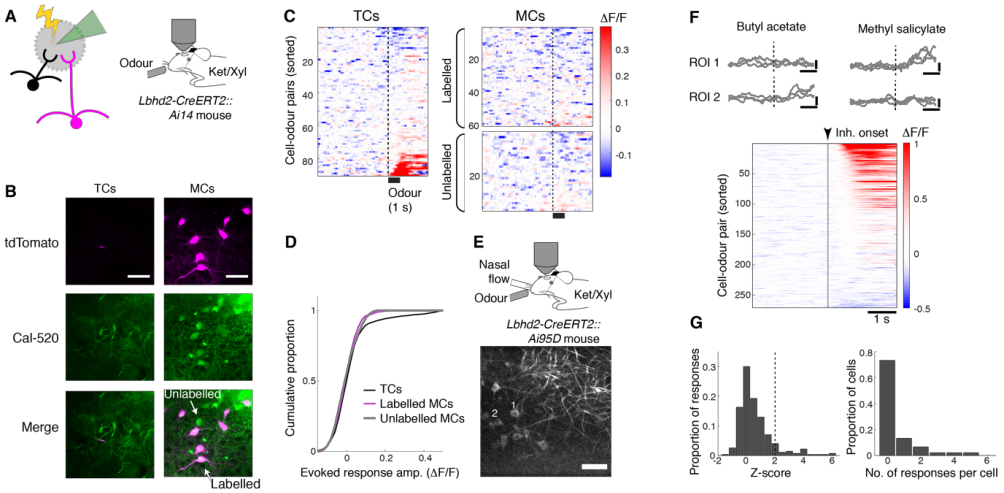


**Figure 10:** *Odour response properties of labelled MCs, in comparison to TCs*

(**A**) Schematic showing low intensity electroporation of Cal-520 dextran solution in the glomerular layer. (**B**) MCs were those located ~ 300 μm below the brain surface, red fluorescence is pseudocoloued magenta (labeled = red fluorescent cells + green fluorescence, unlabeled = loaded cells without red fluorescence), while TCs were smaller cells located more superficially. Strongly fluorescent cells were excluded from analysis. Scale bar = 50 μm. (**C**) Normalised fluorescence (ΔF/F) from TCs (left) and labeled and unlabeled MCs (right, top and bottom, respectively), shown as colormap (n = 2 mice). Excitatory responses are more prevalent in TCs. Cal-520 has a lower affinity to $Ca^{2+}$ than GCaMP6 variants, which may make hyperpolarizing responses to odours less detectable. (**D**) Cumulative histogram of response amplitude, for TCs (black), labeled MCs (magenta) and unlabeled MCs (grey). Overall distributions are not significantly different (two-sample K-S test; p = 0.56). (**E**) Top, experimental configuration; bottom, example field of view at a depth ~280 μm below the brain surface. Scale bar = 50 μm. (**F**) Top, example transients from two ROIs indicated in (**E**). Scale bars, vertical = 0.5 ΔF/F, horizontal = 1 s. Dotted line represents onset of the first inhalation after final valve opening. Bottom, summary of fluorescence change in response to odour presentations shown with a colormap (n = 228 cell-odour pairs, 38 cells, 3 mice). (**G**) Summary statistics of evoked responses; left, histogram of mean fluorescence change during odour (1 s from inhalation onset) expressed as Z-score for the data in (**E**); right, number of odours that each cell responds with a fluorescence increase (z-score greater than 2).

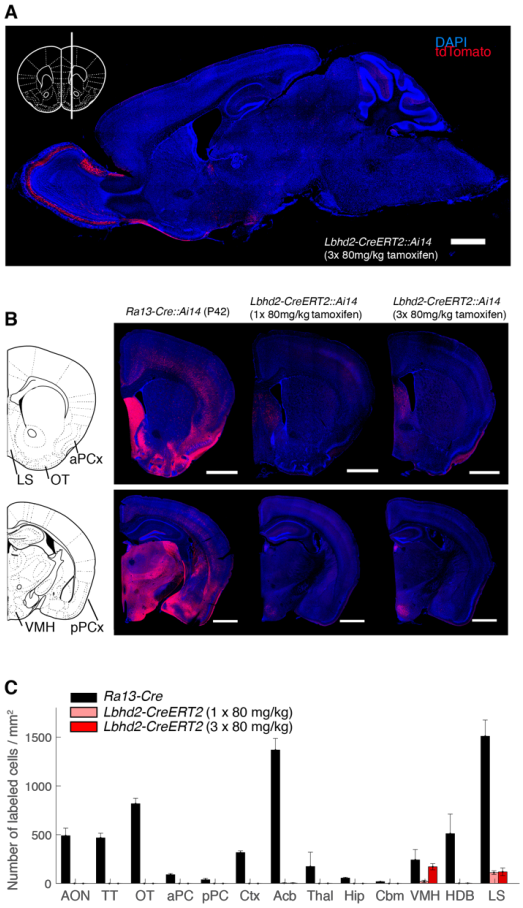


**Figure 11**: *Brain-wide labeling is significantly reduced in the Lbhd2-CreERT2 line.*
(**A**) A sagittal view of an example brain from a P42 Lbhd-CreERT2 mouse, which received 3 doses of tamoxifen (80 mg.kg$^{-1}$) at P21, showing DAPI (blue) and tdTomato (red) signals. Inset shows the medio-lateral plane for the sagittal section. Scale bar = 1 mm. (**B**) Example coronal images from *Ra13::Ai14* (left), and *Lbhd2-IRES-CreERT2::Ai14* mice that received 1 x tamoxifen and 3 x tamoxifen doses (middle and right, respectively). Illustrations on the left depict corresponding anatomical borders at this plane. Scale bar = 1 mm. (**C**) Summary showing average density of labelled cells for each anatomical region (n = 3 mice per region). Acb = Accumbens Nucleus (shell); AON = anterior olfactory nucleus; Cbm = cerebellum; Ctx = cerebral cortex; aPCx = anterior piriform cortex; HDB = nucleus of the horizontal limb of the diagonal band; Hip = hippocampus; LS = lateral septum; OT = olfactory tubercle; pPCx = posterior piriform cortex; Thal = thalamus; TT = tenia tecta; VMH = ventromedial nucleus of the hypothalamus.

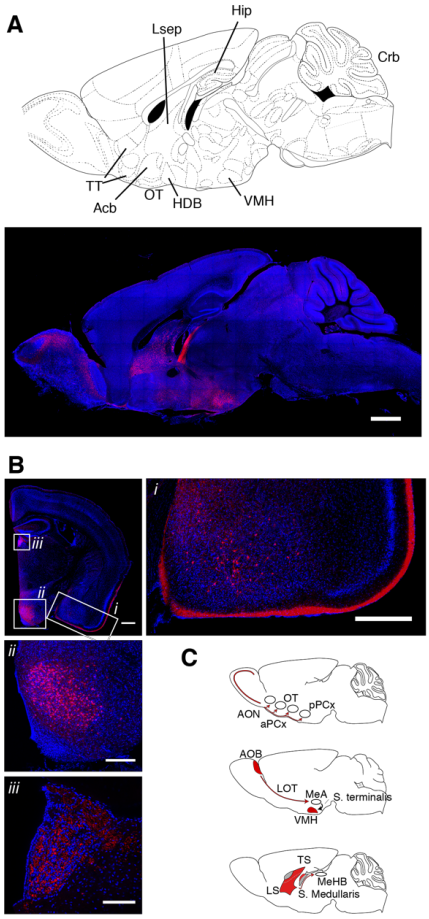


**Figure 12:** *Recombination pattern outside of the OB in Lbhd2-CreERT2 mice*
(A) A confocal image at a sagittal plane about 0.36 mm from the midline in a Lbhd2-CreERT2::Ai14 mouse. Scale bar = 1 mm. (**B**) Coronal view at ~1.46 mm posterior to the Bregma, showing (i) labelled cells in the basolateral amygdaloid nucleus, fibre endings in the molecular layer medial amygdaloid nucleus and posterior piriform cortex; (ii) densely labelled somata in the ventromedial nucleus of the hypothalamus and (iii) labelled fibres in the medial habenular nucleus. (**C**) Summary of labelled structures with respect to distinct pathways; Top, MCs of the main olfactory bulb are labelled, but not their cortical targets. Middle; principal neurons of the accessory olfactory bulb are labelled. Labelled fibres, but not somata, are visible in the medial amygdaloid nucleus. The target of the medial amygdaloid nucleus, namely, the ventromedial nucleus of the hypothalamus, has densely labelled cells. Bottom, lateral septum densely contains labelled cells; the output fiber tracts are strongly labelled (stria medullaris), and labelled fibres are clearly visible in the target structure, namely, the medial habenular nucleus.

842 Table 2: *List of genes differentially expressed between mitral cells and tufted cells.*
843

| Gene Name | Mean Expression (log2(count+1)) | Adjusted p value |
|---|---|---|
| Myh8 | 2.14 | 1.57E-09 |
| Pkib | 3.40 | 7.02E-06 |
| Fxyd7 | 3.66 | 1.41E-05 |
| A230065H16Rik (Ldbh2) | 3.77 | 1.55E-05 |
| Ebf1 | 2.55 | 1.55E-05 |
| Calb2 | 4.60 | 1.55E-05 |
| Snca | 5.10 | 1.55E-05 |
| C1ql1 | 2.53 | 1.55E-05 |
| Cxcl14 | 0.42 | 1.55E-05 |
| Sostdc1 | 0.36 | 2.07E-05 |
| Tmsb10 | 6.12 | 3.05E-05 |
| Spp1 | 2.20 | 3.45E-05 |
| Ntng1 | 4.76 | 4.25E-05 |
| RP23-407N2.2 | 1.81 | 4.70E-05 |
| 1110008P14Rik | 2.45 | 0.000163822 |
| Tspan17 | 1.99 | 0.000211554 |
| Uchl1 | 3.24 | 0.000253744 |
| Shisa3 | 1.98 | 0.000253744 |
| Gap43 | 3.69 | 0.000439148 |
| Ppm1j | 1.85 | 0.000449468 |
| Rph3a | 0.74 | 0.000449468 |
| Crtac1 | 1.97 | 0.000449468 |
| Tnnc1 | 0.27 | 0.000457871 |
| Mmp17 | 0.45 | 0.000585813 |
| Nov | 0.18 | 0.000707168 |
| Gng13 | 1.03 | 0.001406527 |
| Rab15 | 1.62 | 0.001959665 |
| Gm27199 | 1.11 | 0.001978521 |
| Vsnl1 | 0.83 | 0.002521565 |
| Stmn2 | 3.57 | 0.003524909 |
| Npr1 | 1.30 | 0.003848843 |
| Doc2g | 4.52 | 0.004924184 |
| Nptxr | 0.78 | 0.005760704 |
| Kcnq3 | 0.94 | 0.005928465 |
| Slc1a2 | 1.29 | 0.007685702 |

| | | |
|---|---|---|
| Sncb | 4.97 | 0.00781742 |
| Ephx4 | 1.37 | 0.009259688 |
| Atp9a | 1.91 | 0.009383075 |
| Nrsn1 | 2.65 | 0.01005383 |
| Diras2 | 1.50 | 0.01094975 |
| Rgs4 | 0.76 | 0.01098611 |
| AI413582 | 2.09 | 0.0124281 |
| Abi3bp | 0.09 | 0.01393499 |
| Lingo1 | 1.67 | 0.01393499 |
| Tshz2 | 3.22 | 0.01393499 |
| Mal2 | 0.18 | 0.01393499 |
| Fkbp1b | 0.00 | 0.01393499 |
| Prkcb | 1.23 | 0.01504482 |
| Cdh4 | 1.02 | 0.01504482 |
| Meg3 | 7.01 | 0.01660475 |
| Chrna3 | 0.61 | 0.01660475 |
| Ifitm10 | 0.74 | 0.01905793 |
| Adk | 0.34 | 0.02020242 |
| Stx1a | 0.89 | 0.02020242 |
| Igfbp5 | 2.75 | 0.02381658 |
| Fam19a1 | 0.09 | 0.0261028 |
| Grin1os | 0.09 | 0.0261028 |
| Cdc20 | 0.09 | 0.0261028 |
| Gm26803 | 0.09 | 0.0261028 |
| Resp18 | 1.14 | 0.0261028 |
| Pantr1 | 1.12 | 0.02678842 |
| Lmo4 | 0.91 | 0.02690157 |
| Pvrl1 | 1.07 | 0.03585761 |
| Kitl | 0.00 | 0.0397583 |

844
845

## References


Ackels T, Jordan R, Schaefer AT, Fukunaga I (2020) Respiration-Locking of Olfactory Receptor and Projection Neurons in the Mouse Olfactory Bulb and Its Modulation by Brain State. Frontiers in Cellular Neuroscience 14.

Antal M, Eyre M, Finklea B, Nusser Z (2006) External tufted cells in the main olfactory bulb form two distinct subpopulations. Eur J Neurosci 24:1124-1136.

Birnbaum KD (2018) Power in Numbers: Single-Cell RNA-Seq Strategies to Dissect Complex Tissues. Annual Review of Genetics 52:203-221.

Bochkov YA, Palmenberg AC (2006) Translational efficiency of EMCV IRES in bicistronic vectors is dependent upon IRES sequence and gene location. Biotechniques 41:283-292.

Burton SD (2017) Inhibitory circuits of the mammalian main olfactory bulb. Journal of Neurophysiology 118:2034-2051.

Burton SD, Urban NN (2014) Greater excitability and firing irregularity of tufted cells underlies distinct afferent-evoked activity of olfactory bulb mitral and tufted cells. The Journal of Physiology 592:2097-2118.

Campello RJGB, Moulavi D, Sander J (2013) Density-Based Clustering Based on Hierarchical Density Estimates. In: Advances in Knowledge Discovery and Data Mining (Pei J, Tseng VS, Cao L, Motoda H, Xu G, eds), pp 160-172: Springer Berlin Heidelberg.

Chong E, Moroni M, Wilson C, Shoham S, Panzeri S, Rinberg D (2020) Manipulating synthetic optogenetic odors reveals the coding logic of olfactory perception. Science 368:eaba2357.

Cong L, Ran FA, Cox D, Lin S, Barretto R, Habib N, Hsu PD, Wu X, Jiang W, Marraffini LA, Zhang F (2013) Multiplex Genome Engineering Using CRISPR/Cas Systems. Science 339:819.

Cruz-Martín A, El-Danaf RN, Osakada F, Sriram B, Dhande OS, Nguyen PL, Callaway EM, Ghosh A, Huberman AD (2014) A dedicated circuit links direction-selective retinal ganglion cells to the primary visual cortex. Nature 507:358-361.

Daigle TL et al. (2018) A Suite of Transgenic Driver and Reporter Mouse Lines with Enhanced Brain-Cell-Type Targeting and Functionality. Cell 174:465-480.e422.

Dhande OS, Estevez ME, Quattrochi LE, El-Danaf RN, Nguyen PL, Berson DM, Huberman AD (2013) Genetic Dissection of Retinal Inputs to Brainstem Nuclei Controlling Image Stabilization. The Journal of Neuroscience 33:17797.

Economo MN, Hansen KR, Wachowiak M (2016) Control of Mitral/Tufted Cell Output by Selective Inhibition among Olfactory Bulb Glomeruli. Neuron 91:397-411.

881 Eiting TP, Wachowiak M (2020) Differential Impacts of Repeated Sampling on Odor Representations by
882 Genetically-Defined Mitral and Tufted Cell Subpopulations in the Mouse Olfactory Bulb. The
883 Journal of Neuroscience 40:6177.

884 Faedo A, Ficara F, Ghiani M, Aiuti A, Rubenstein JLR, Bulfone A (2002) Developmental expression of the
885 T-box transcription factor T-bet/Tbx21 during mouse embryogenesis. Mechanisms of
886 Development 116:157-160.

887 Feil R, Wagner J, Metzger D, Chambon P (1997) Regulation of Cre Recombinase Activity by Mutated
888 Estrogen Receptor Ligand-Binding Domains. Biochemical and Biophysical Research
889 Communications 237:752-757.

890 Fischer KB, Collins HK, Callaway EM (2019) Sources of off-target expression from recombinase-
891 dependent AAV vectors and mitigation with cross-over insensitive ATG-out vectors. Proceedings
892 of the National Academy of Sciences 116:27001.

893 Fukunaga I, Berning M, Kollo M, Schmaltz A, Schaefer Andreas T (2012) Two Distinct Channels of
894 Olfactory Bulb Output. Neuron 75:320-329.

895 Geramita MA, Burton SD, Urban NN (2016) Distinct lateral inhibitory circuits drive parallel processing of
896 sensory information in the mammalian olfactory bulb. eLife 5:e16039.

897 Gong S, Doughty M, Harbaugh CR, Cummins A, Hatten ME, Heintz N, Gerfen CR (2007) Targeting Cre
898 Recombinase to Specific Neuron Populations with Bacterial Artificial Chromosome Constructs.
899 The Journal of Neuroscience 27:9817.

900 Gong S, Zheng C, Doughty ML, Losos K, Didkovsky N, Schambra UB, Nowak NJ, Joyner A, Leblanc G,
901 Hatten ME, Heintz N (2003) A gene expression atlas of the central nervous system based on
902 bacterial artificial chromosomes. Nature 425:917-925.

903 Haberly LB, Price JL (1977) The axonal projection patterns of the mitral and tufted cells of the olfactory
904 bulb in the rat. Brain Research 129:152-157.

905 Haddad R, Lanjuin A, Madisen L, Zeng H, Murthy VN, Uchida N (2013) Olfactory cortical neurons read out
906 a relative time code in the olfactory bulb. Nature Neuroscience 16:949.

907 Hayar A, Karnup S, Ennis M, Shipley MT (2004) External Tufted Cells: A Major Excitatory Element That
908 Coordinates Glomerular Activity. The Journal of Neuroscience 24:6676.

909 Heintz N (2004) Gene Expression Nervous System Atlas (GENSAT). Nature Neuroscience 7:483-483.

910 Hovis KR, Padmanabhan K, Urban NN (2010) A simple method of in vitro electroporation allows
911 visualization, recording, and calcium imaging of local neuronal circuits. Journal of Neuroscience
912 Methods 191:1-10.

913 Igarashi KM, Ieki N, An M, Yamaguchi Y, Nagayama S, Kobayakawa K, Kobayakawa R, Tanifuji M, Sakano
914 H, Chen WR, Mori K (2012) Parallel Mitral and Tufted Cell Pathways Route Distinct Odor
915 Information to Different Targets in the Olfactory Cortex. The Journal of Neuroscience 32:7970.

916 Imamura F, Ayoub AE, Rakic P, Greer CA (2011) Timing of neurogenesis is a determinant of olfactory
917 circuitry. Nature Neuroscience 14:331-337.

918 Jordan R, Fukunaga I, Kollo M, Schaefer AT (2018) Active Sampling State Dynamically Enhances Olfactory
919 Bulb Odor Representation. Neuron 98:1214-1228.e1215.

920 Kapoor V, Provost AC, Agarwal P, Murthy VN (2016) Activation of raphe nuclei triggers rapid and distinct
921 effects on parallel olfactory bulb output channels. Nature Neuroscience 19:271.

922 Kobak D, Berens P (2019) The art of using t-SNE for single-cell transcriptomics. Nature Communications
923 10:5416.

924 Larsson LI, Rehfeld JF (1979) Localization and molecular heterogeneity of cholecystokinin in the central
925 and peripheral nervous system. Brain Research 165:201-218.

926 Lein E, Borm LE, Linnarsson S (2017) The promise of spatial transcriptomics for neuroscience in the era
927 of molecular cell typing. Science 358:64.

928 Lein ES et al. (2006) Genome-wide atlas of gene expression in the adult mouse brain. Nature 445:168.

929 Lein ES et al. (2007) Genome-wide atlas of gene expression in the adult mouse brain. Nature 445:168-
930 176.

931 Li H, Horns F, Wu B, Xie Q, Li J, Li T, Luginbuhl DJ, Quake SR, Luo L (2017) Classifying Drosophila Olfactory
932 Projection Neuron Subtypes by Single-Cell RNA Sequencing. Cell 171:1206-1220.e1222.

933 Lim L, Pakan JMP, Selten MM, Marques-Smith A, Llorca A, Bae SE, Rochefort NL, Marín O (2018)
934 Optimization of interneuron function by direct coupling of cell migration and axonal targeting.
935 Nature Neuroscience 21:920-931.

936 Luo L, Callaway EM, Svoboda K (2018) Genetic Dissection of Neural Circuits: A Decade of Progress.
937 Neuron 98:256-281.

938 Macrides F, Schneider SP (1982) Laminar organization of mitral and tufted cells in the main olfactory
939 bulb of the adult hamster. Journal of Comparative Neurology 208:419-430.

940 Madisen L, Zwingman TA, Sunkin SM, Oh SW, Zariwala HA, Gu H, Ng LL, Palmiter RD, Hawrylycz MJ,
941 Jones AR, Lein ES, Zeng H (2010) A robust and high-throughput Cre reporting and
942 characterization system for the whole mouse brain. Nature Neuroscience 13:133-140.

943 Madisen L et al. (2012) A toolbox of Cre-dependent optogenetic transgenic mice for light-induced
944 activation and silencing. Nature Neuroscience 15:793.

945 Madisen L et al. (2015) Transgenic Mice for Intersectional Targeting of Neural Sensors and Effectors with
946 High Specificity and Performance. Neuron 85:942-958.

947 Masland RH (2004) Neuronal cell types. Current Biology 14:R497-R500.

948 Mitsui S, Igarashi KM, Mori K, Yoshihara Y (2011) Genetic visualization of the secondary olfactory
949 pathway in Tbx21 transgenic mice. Neural Systems & Circuits 1:5.

950 Mizuguchi R, Naritsuka H, Mori K, Yoshihara Y (2012) Tbr2 Deficiency in Mitral and Tufted Cells Disrupts
951 Excitatory–Inhibitory Balance of Neural Circuitry in the Mouse Olfactory Bulb. The Journal of
952 Neuroscience 32:8831.

953 Mizuno S, Dinh TTH, Kato K, Mizuno-Iijima S, Tanimoto Y, Daitoku Y, Hoshino Y, Ikawa M, Takahashi S,
954 Sugiyama F, Yagami K-i (2014) Simple generation of albino C57BL/6J mice with G291T mutation
955 in the tyrosinase gene by the CRISPR/Cas9 system. Mammalian Genome 25:327-334.

956 Mori K, Kishi K, Ojima H (1983) Distribution of dendrites of mitral, displaced mitral, tufted, and granule
957 cells in the rabbit olfactory bulb. Journal of Comparative Neurology 219:339-355.

958 Münch TA, da Silveira RA, Siegert S, Viney TJ, Awatramani GB, Roska B (2009) Approach sensitivity in the
959 retina processed by a multifunctional neural circuit. Nature Neuroscience 12:1308-1316.

960 Nagai Y, Sano H, Yokoi M (2005) Transgenic expression of Cre recombinase in mitral/tufted cells of the
961 olfactory bulb. genesis 43:12-16.

962 Nagayama S, Enerva A, Fletcher M, Masurkar A, Igarashi K, Mori K, Chen W (2010) Differential Axonal
963 Projection of Mitral and Tufted Cells in the Mouse Main Olfactory System. Frontiers in Neural
964 Circuits 4:120.

965 Otazu Gonzalo H, Chae H, Davis Martin B, Albeanu Dinu F (2015) Cortical Feedback Decorrelates
966 Olfactory Bulb Output in Awake Mice. Neuron 86:1461-1477.

967 Papaioannou VE, Silver LM (1998) The T-box gene family. BioEssays 20:9-19.

968 Pashkovski SL, Iurilli G, Brann D, Chicharro D, Drummey K, Franks KM, Panzeri S, Datta SR (2020)
969 Structure and flexibility in cortical representations of odour space. Nature 583:253-258.

970 Pfeffer CK, Xue M, He M, Huang ZJ, Scanziani M (2013) Inhibition of inhibition in visual cortex: the logic
971 of connections between molecularly distinct interneurons. Nature Neuroscience 16:1068.

972 Phillips ME, Sachdev RNS, Willhite DC, Shepherd GM (2012) Respiration Drives Network Activity and
973 Modulates Synaptic and Circuit Processing of Lateral Inhibition in the Olfactory Bulb. The Journal
974 of Neuroscience 32:85.

975 Rothermel M, Brunert D, Zabawa C, Díaz-Quesada M, Wachowiak M (2013) Transgene Expression in
976 Target-Defined Neuron Populations Mediated by Retrograde Infection with Adeno-Associated
977 Viral Vectors. The Journal of Neuroscience 33:15195.

978 Sanes JR, Masland RH (2015) The Types of Retinal Ganglion Cells: Current Status and Implications for
979 Neuronal Classification. Annual Review of Neuroscience 38:221-246.

980 Schwarz D, Kollo M, Bosch C, Feinauer C, Whiteley I, Margrie TW, Cutforth T, Schaefer AT (2018)
981 Architecture of a mammalian glomerular domain revealed by novel volume electroporation
982 using nanoengineered microelectrodes. Nature Communications 9:183.

983 Seroogy KB, Brecha N, Gall C (1985) Distribution of cholecystokinin-like immunoreactivity in the rat main
984 olfactory bulb. Journal of Comparative Neurology 239:373-383.

985 Shekhar K, Lapan SW, Whitney IE, Tran NM, Macosko EZ, Kowalczyk M, Adiconis X, Levin JZ, Nemesh J,
986 Goldman M, McCarroll SA, Cepko CL, Regev A, Sanes JR (2016) Comprehensive Classification of
987 Retinal Bipolar Neurons by Single-Cell Transcriptomics. Cell 166:1308-1323.e1330.

988 Short SM, Wachowiak M (2019) Temporal Dynamics of Inhalation-Linked Activity across Defined
989 Subpopulations of Mouse Olfactory Bulb Neurons Imaged *In Vivo*. eneuro 6:ENEURO.0189-
990 0119.2019.

991 Ståhl PL et al. (2016) Visualization and analysis of gene expression in tissue sections by spatial
992 transcriptomics. Science 353:78.

993 Stowers L, Liberles SD (2016) State-dependent responses to sex pheromones in mouse. Current Opinion
994 in Neurobiology 38:74-79.

995 Sugino K, Hempel CM, Miller MN, Hattox AM, Shapiro P, Wu C, Huang ZJ, Nelson SB (2006) Molecular
996 taxonomy of major neuronal classes in the adult mouse forebrain. Nature Neuroscience 9:99-
997 107.

998 Takahashi N, Ebner C, Sigl-Glöckner J, Moberg S, Nierwetberg S, Larkum ME (2020) Active dendritic
999 currents gate descending cortical outputs in perception. Nature Neuroscience 23:1277-1285.

1000 Tang F, Barbacioru C, Wang Y, Nordman E, Lee C, Xu N, Wang X, Bodeau J, Tuch BB, Siddiqui A, Lao K,
1001 Surani MA (2009) mRNA-Seq whole-transcriptome analysis of a single cell. Nature Methods
1002 6:377.

1003 Taniguchi H, He M, Wu P, Kim S, Paik R, Sugino K, Kvitsani D, Fu Y, Lu J, Lin Y, Miyoshi G, Shima Y, Fishell
1004 G, Nelson Sacha B, Huang ZJ (2011) A Resource of Cre Driver Lines for Genetic Targeting of
1005 GABAergic Neurons in Cerebral Cortex. Neuron 71:995-1013.

1006 Tasic B et al. (2016) Adult mouse cortical cell taxonomy revealed by single cell transcriptomics. Nature
1007 Neuroscience 19:335.

1008 van der Maaten L, Hinton G (2008) Visualizing Data using t-SNE. Journal of Machine Learning Researcch
1009 9:2579-2605.

1010 Wang F, Flanagan J, Su N, Wang L-C, Bui S, Nielson A, Wu X, Vo H-T, Ma X-J, Luo Y (2012) RNAscope: a
1011 novel in situ RNA analysis platform for formalin-fixed, paraffin-embedded tissues. J Mol Diagn
1012 14:22-29.

1013 Wolff SBE, Gründemann J, Tovote P, Krabbe S, Jacobson GA, Müller C, Herry C, Ehrlich I, Friedrich RW,
1014 Letzkus JJ, Lüthi A (2014) Amygdala interneuron subtypes control fear learning through
1015 disinhibition. Nature 509:453.

1016 Zeisel A, Muñoz-Manchado AB, Codeluppi S, Lönnerberg P, La Manno G, Juréus A, Marques S, Munguba
1017 H, He L, Betsholtz C, Rolny C, Castelo-Branco G, Hjerling-Leffler J, Linnarsson S (2015) Cell types
1018 in the mouse cortex and hippocampus revealed by single-cell RNA-seq. Science 347:1138.

1019 Zeisel A, Hochgerner H, Lönnerberg P, Johnsson A, Memic F, van der Zwan J, Häring M, Braun E, Borm LE,
1020 La Manno G, Codeluppi S, Furlan A, Lee K, Skene N, Harris KD, Hjerling-Leffler J, Arenas E, Ernfors
1021 P, Marklund U, Linnarsson S (2018) Molecular Architecture of the Mouse Nervous System. Cell
1022 174:999-1014.e1022.

1023 Zeng H, Sanes JR (2017) Neuronal cell-type classification: challenges, opportunities and the path
1024 forward. Nature Reviews Neuroscience 18:530.

1025 Zeppilli S, Ackels T, Attey R, Klimpert N, Boeing S, Crombach A, Schaefer A, Fleischmann A (2020)
1026 Molecular characterization of projection neuron subtypes in the mouse olfactory bulb.
1027 bioRxiv:2020.2011.2030.405571.
1028